CHAPTER 3

Results and discussion

3.1 Sonochemical synthesis, photocatalysis and photonic properties of Ce-doped ZnO nanostructures

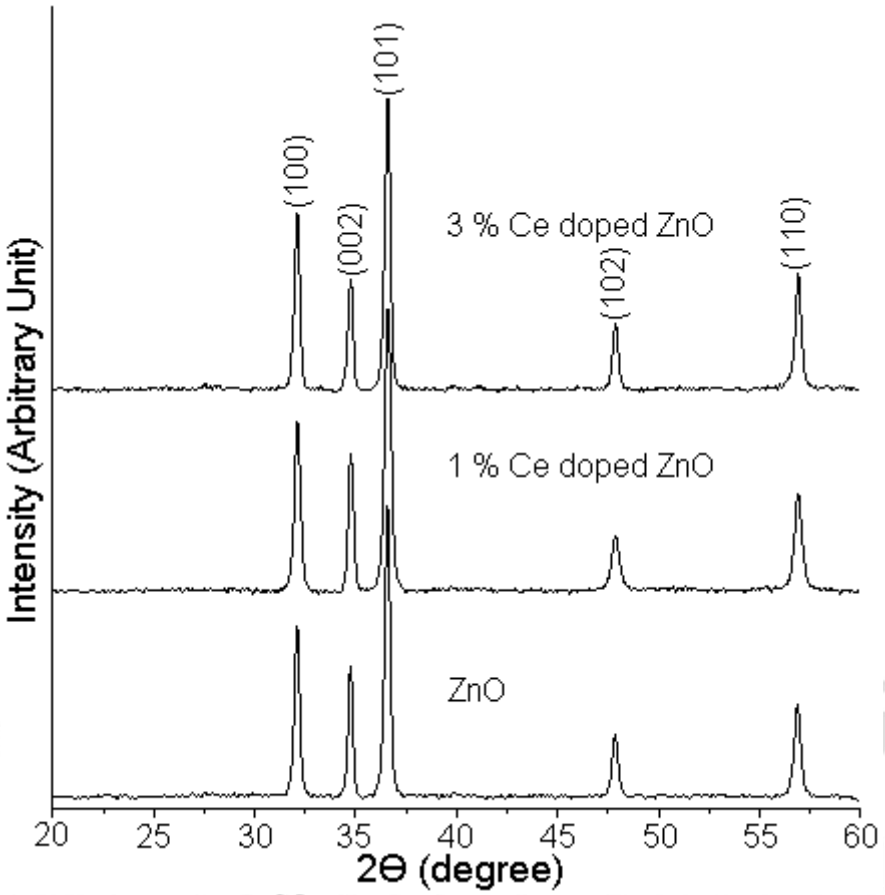

Figure 3.1 XRD patterns of 0-3% Ce-doped ZnO synthesized by sonochemical method.

Figure 3.1 shows XRD patterns of Ce-doped ZnO with different Ce^{3+} contents. The XRD pattern of pure ZnO powders shows peaks at 2θ = 32.11, 34.75, 36.59, 47.85 and 56.93 degrees corresponding to the (100), (002), (101), (102) and (110) planes of hexagonal wurtzite ZnO structure with agreement to JCPDS No. 36-1451 [34]. By

doping Ce^{3+} in ZnO, only the ZnO peaks were still detected. No diffraction peaks of doping atoms or other phases were detected, indicating that the Ce^{3+} ions completely substituted for Zn^{2+} ions in ZnO lattice. Ce^{3+} concentration could be too low to be detected by XRD.

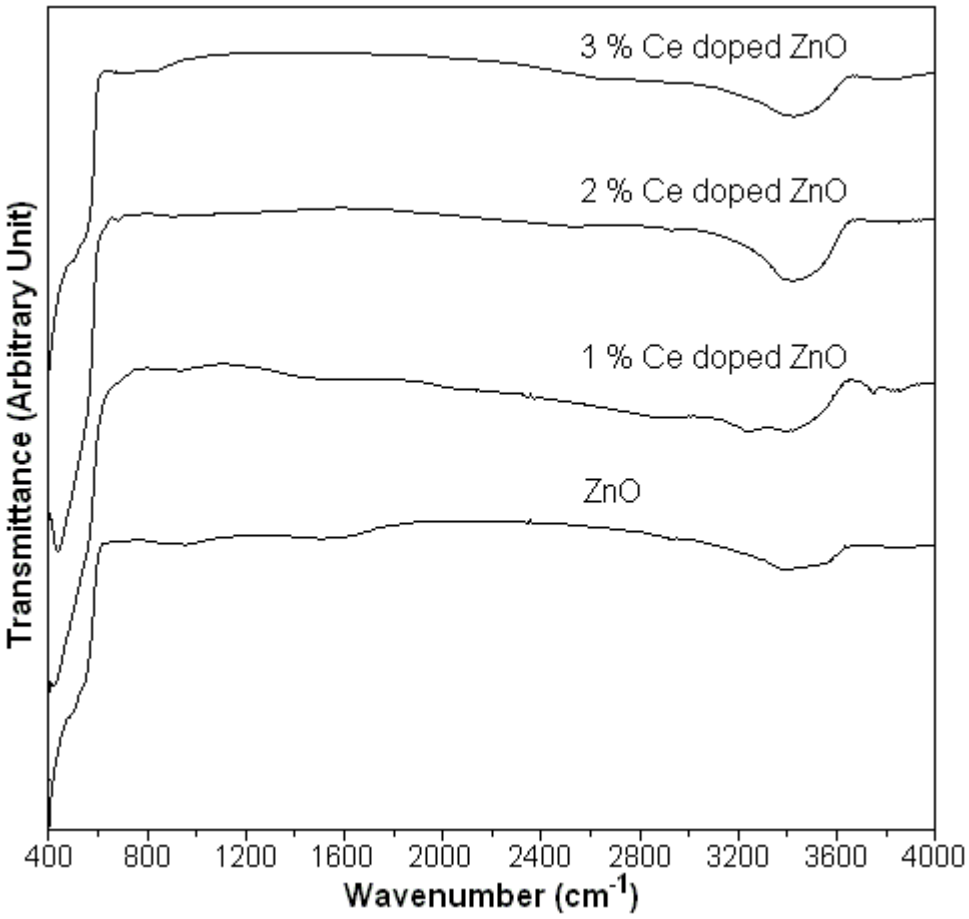

Figure 3.2 FTIR spectra of 0-3% Ce-doped ZnO synthesized by sonochemical method.

FTIR spectra (Figure 3.2) of the 0-3% Ce-doped ZnO, analyzed over the wavenumber of 400-4000 cm^{-1}, show strong bands at around 450-500 cm^{-1} with one broad band at 3300-3600 cm^{-1}. In this research, pure ZnO and 1–3% Ce-doped ZnO show the same strong absorption bands at 426 cm^{-1} with the shoulders at 565 cm^{-1}, assigned as E_{2H} vibration and oxygen vacancies of wurtzite ZnO crystal, respectively [35]. For every two Ce^{3+} ions doped into ZnO crystal, one O^{2-} vacancy formed to maintain electroneutrality of the crystal. Considering the ionic radii of Zn^{2+} (0.074 nm) and Ce^{3+} (0.102 nm) [36-38], it was likely that Ce^{3+} partially substituted for Zn^{2+} in the ZnO crystal. An absorption bands at 3300–3600 cm^{-1} is the O–H stretching vibration of

adsorbed water on the sample surface. The corresponding spectrum of the doping material did not exhibit such absorbance implying that the synthesized products are ZnO, in accordance with the XRD analysis [11].

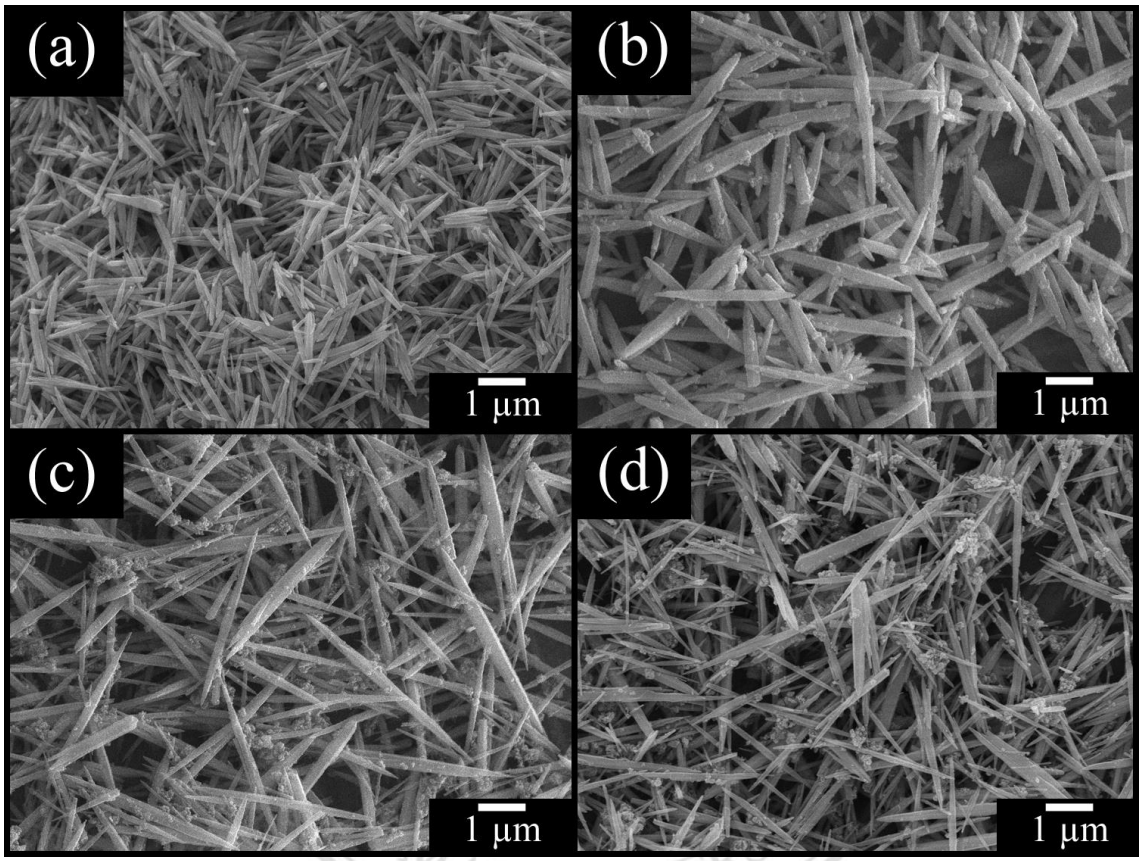

Figure 3.3 SEM image of (a) pure ZnO, (b) 1% Ce-doped ZnO, (c) 2% Ce-doped ZnO and (d) 3% Ce-doped ZnO, respectively.

Figure 3.3 shows FESEM images of ZnO samples at different contents of Ce doping synthesized by sonochemical method at pH 9.5. Pure ZnO (Figure 3.3 (a)) was nanoneedle-like particles with sharp tips on both ends. A base width at the middle and tapered tips were 100 nm and 25 nm with 1 μm long. By doping with Ce (Figure 3.3 (b)–(d)), the morphology of 1–3% Ce-doped ZnO remained as nanoneedles, but their lengths were increased to 2–3 μm.

The element distributions of the Ce-doped ZnO nanoneedle were determined using energy dispersive X-ray spectroscopy (EDX) as shown in Figure 3.4. The EDX spectrum of 3% Ce-doped ZnO was detected Zn, O and Ce elements. It can seen that Ce element was good distribute in ZnO sample.

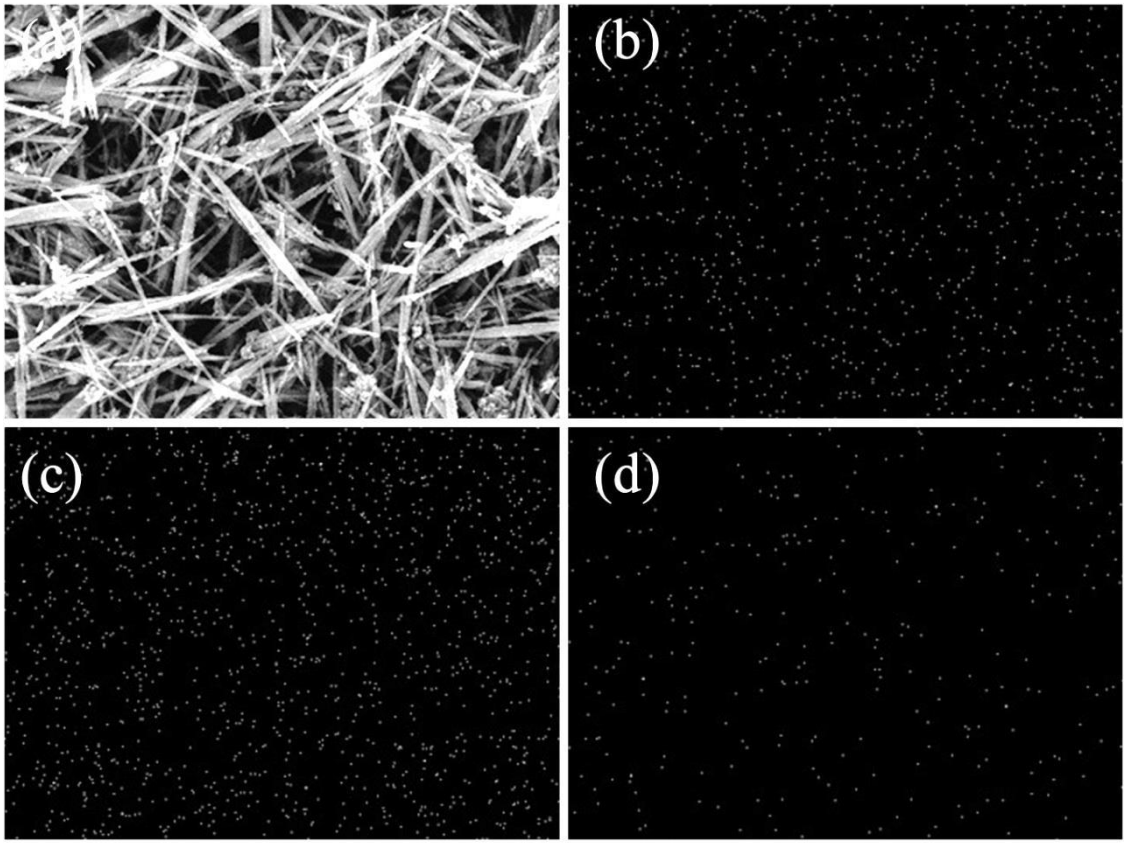

Figure 3.4 (a) SEM image and EDX mapping of (b) Zn, (c) O and (d) Ce elements of as-synthesized 3% Ce-doped ZnO sample.

TEM and HRTEM images and SAED pattern (Figure 3.5 (a) and (b)) represent phase and morphology of pure ZnO nanoneedles with 800 nm long, uniform diameter and slightly rough surface. The HRTEM image was analyzed on edge part of a typical ZnO nanoneedle. The (002) fringe at right angle to the [001] growth direction with 2.61 Å apart were detected, in consistent with that of the bulk wurtzite ZnO crystal. Some defects were also detected. The SAED pattern shows a bright spot pattern of single crystal of hexagonal ZnO. Consider the 3% Ce-doped ZnO images and SAED pattern (Figure 3.5 (c) and (d)), they revealed the straight nanoneedles of single crystal with smooth surface and 80 nm in diameter. The *d*-spacing values measured from the SAED pattern with zone axis of [1–10] are 1.62 Å, 1.38 Å and 2.61 Å, well agree with the (110), (112) and (002) lattice planes of hexagonal ZnO phase, respectively. These indicated that 3% Ce-doped ZnO nanoneedles grew along the [001] direction.

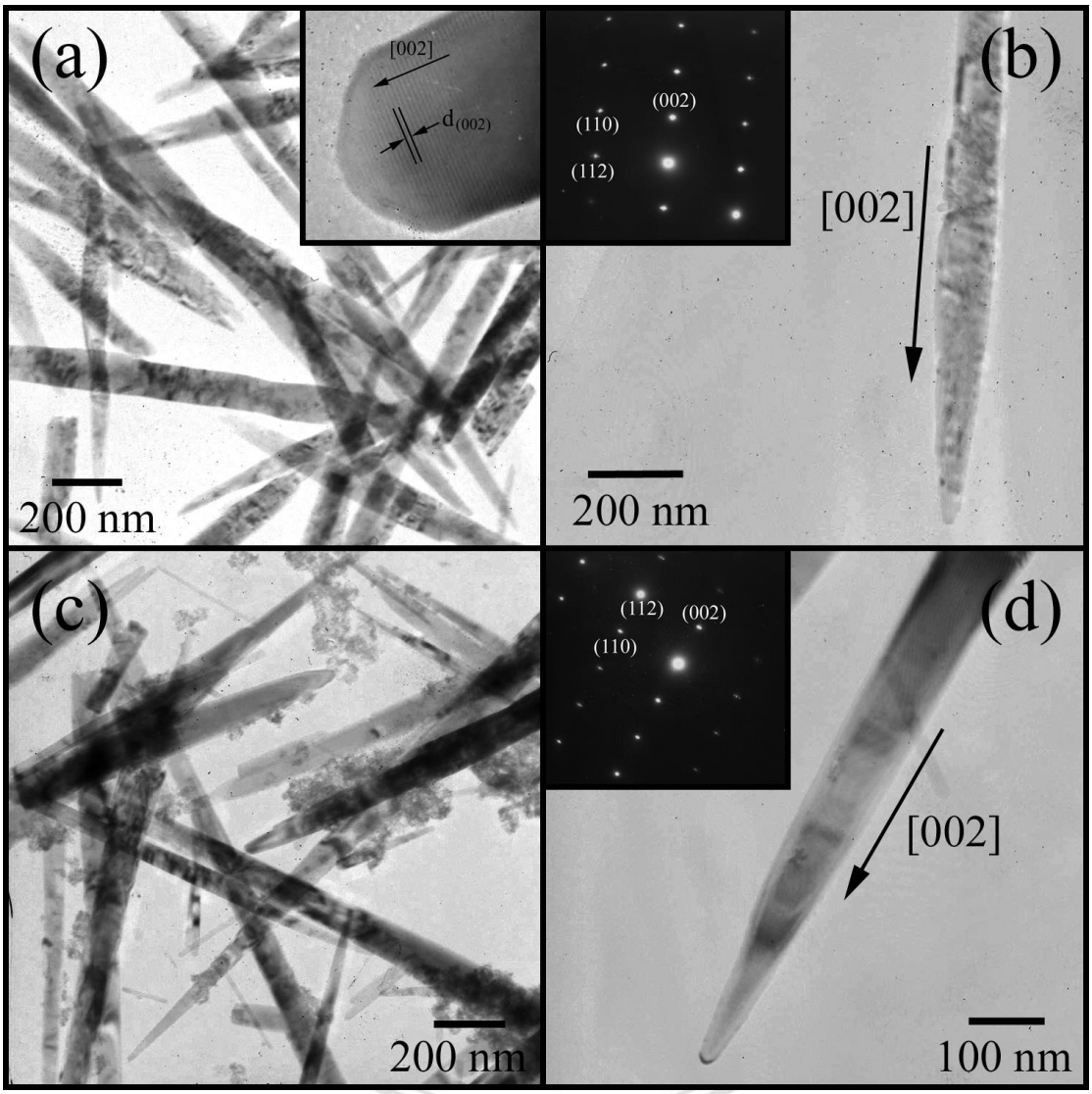

Figure 3.5 TEM images, HRTEM images and SAED patterns of (a, b) ZnO and (c, d) 3% Ce-doped ZnO.

Formation mechanism of ZnO nanoneedles proceeded in a sonochemical bath as follows. First, zincnitrate, water and ammoniumhydroxide absorbed ultrasound energy and followed by the dissociation process to form primary ions. Second, $[Zn(OH)_4]^{2-}$ complex ions formed and further decomposed to give ZnO molecules [15], which nucleated and grew as nanoneedles. Their preferential growth were along the [0001] direction due to the intrinsic anisotropy in growth rate (v) with v[0001] > v[01-10] > v[000-1]. The structure of ZnO single crystal can be described as a number of alternating planes of coordinated Zn^{2+} and O^{2-} ions, the positively charged Zn-(0001) and negatively charged O-(0001) polar surfaces. Due to the decreasing in the

concentration of ZnO_2^{2-} monomers by the rapid nucleation of ZnO, the absorption of OH^- on the positively charged plane dominated the competition of ZnO_2^{2-} growth units. Thus, the OH^- ions stabilized the surface charge of Zn-(0001) to some degree, leading to the formation of nanoneedle-like ZnO along the [0001] direction [39, 40]. When the doping material was also mixed, Ce^{3+} ions diffused and resided in the ZnO nanoneedles.

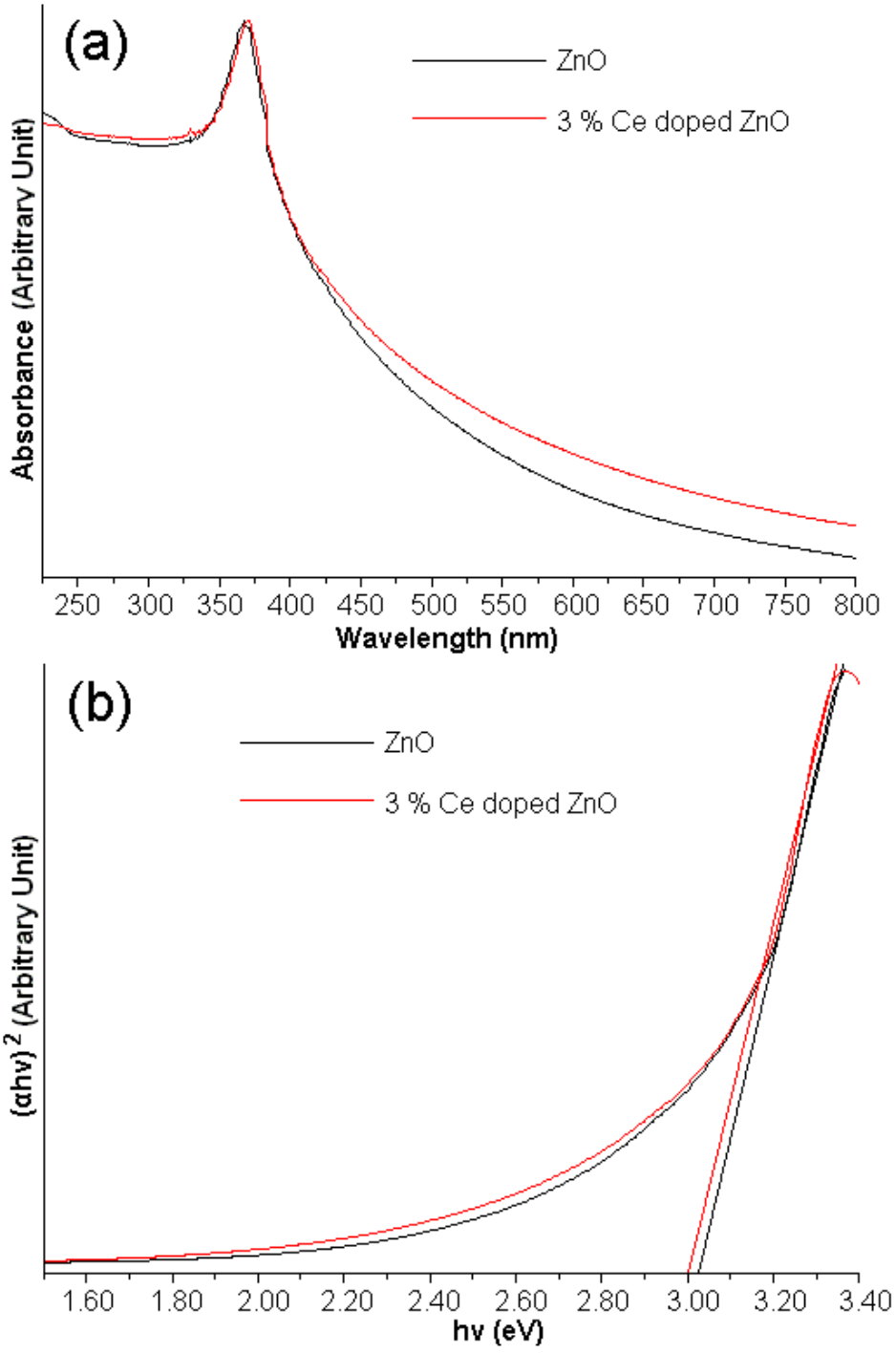

Figure 3.6 (a) UV-visible absorption and (b) $(\alpha h\nu)^2$ vs hν curve of samples.

The optical properties of the ZnO and 3% Ce-doped ZnO were investigated by UV-Visible spectroscopy at room temperature in wavelength of 225-800 nm. The UV-Visible spectra of ZnO as shown in Figure 3.6 (a) present a well defined excitonic absorption peak at 366 nm corresponding to the band-to-band transition [41] while 3% Ce-doped ZnO shows a red shifted absorption at 370 nm as compared to the ZnO sample. Figure 3.6 (b) presents the plotting $(\alpha h\nu)^2$ vs $h\nu$ curve of samples where α is the absorbance, h the Planck constant and ν the frequency. The direct band gap (E_g) of ZnO and 3% Ce-doped ZnO were determined to be at 3.03 and 3.00 eV, respectively.

PL spectra (Figure 3.7) of ZnO with and without Ce doping were studied using 318 nm excitation wavelength. They showed broad emissions in the wavelength range of 325–600 nm. The 3% Ce-doped ZnO showed higher emission intensity than any other products. Upon doing the Gaussian analysis for pure ZnO and 3% Ce-doped ZnO with the highest intensity, the spectra were disintegrated into three emission peaks at 393.1 nm, 442.9 nm and 495.6 nm for pure ZnO, and 392.6 nm, 433.7 nm and 482.2 nm for 3% Ce-doped ZnO corresponding to the UV, blue and blue-green emissions, respectively [29, 42]. The first was caused by the characteristic of near-band-edge emission of free exciton recombination process [43], but the second and third were possibly associated with oxygen vacancies [42] and other defects.

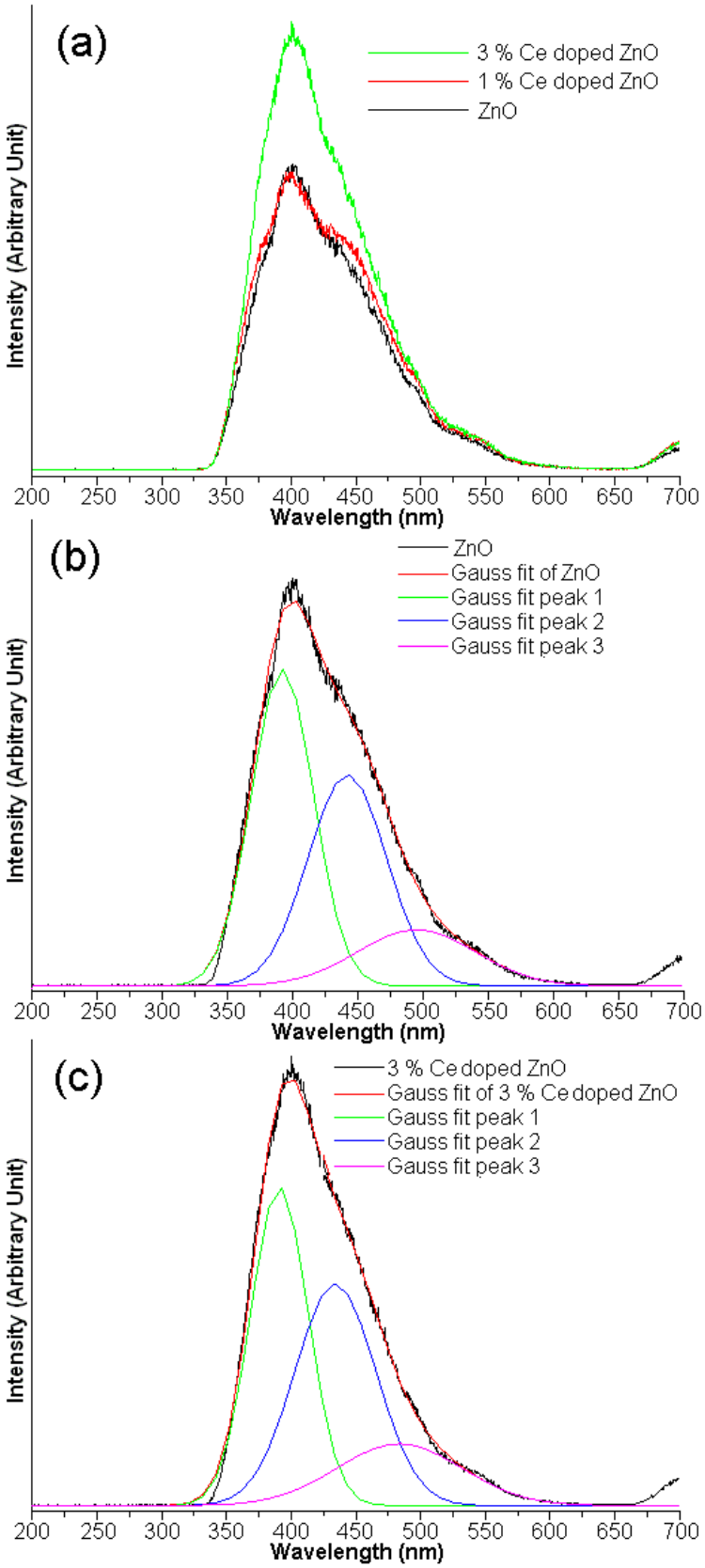

Figure 3.7 (a) PL spectra of ZnO with and without Ce doping. Gaussian analysis of (b) ZnO and (c) 3% Ce-doped ZnO.

Methylene blue (MB) is adopted as a representative organic pollutant to evaluate the photocatalytic performance of the assynthesized Ce-doped ZnO. UV–visible absorbance (Figure 3.8) of undoped ZnO and 3% Ce-doped ZnO during photocatalysis for 0–300 min shows that the absorbance of MB for ZnO was gradually decreased, but that for 3% Ce-doped ZnO was decreased at much faster rate. Figure 3.9 (a) shows the MB degradation rate for ZnO with and without Ce doping under UV light for different lengths of time. Obviously, 3% Ce-doped ZnO shows the most effective in photocatalysis in these solutions. During the first 140 min, MB concentration was rapidly decreased to 32, 70 and 87% for ZnO, 1% Ce-doped ZnO and 3% Ce-doped ZnO, respectively. For 240 min, the MB degradation efficiency for 3% Ce-doped ZnO was higher than 98%, 1.97 times the degradation efficiency of ZnO (49.81%). The higher the concentration of oxygen defects on the surfaces of Ce-doped ZnO nanocrystals is, the stronger the photocatalytic activity will be. Finally, the experimental results presented in this article will be very useful for the research on other metallic/semiconducting catalysts with high catalytic activities.

Photocatalytic activity for degradation of MB obeys the pseudo-first-order reaction kinetics with k as the rate constant and t the UV irradiation time given by

$$C_t = C_o e^{-kt} \quad (3.1)$$

where k is reaction rate constant, Co is the initial concentration of MB and Ct is the concentration of MB after light irradiation [44-46]. Figure 3.9 (b) shows the plots of $\ln(C_0/Ct)$ versus the irradiation time for the photodegradation of MB. In this research, the photodegradation followed very well with the pseudo-first order kinetics with R^2 = 0.9979, 0.9745 and 0.9820 for 0, 1 and 3% Ce-doped ZnO, respectively. The rate constants for degradation of MB on 0, 1 and 3% Ce-doped ZnO are 2.81×10^{-3}, 7.69×10^{-3} and 1.64×10^{-2} min^{-1}, respectively. The rate constants for degradation of MB on 3% Ce-doped ZnO increases the reaction rate about 5.84 times with comparing to pure ZnO. As known as performance activity of photocatalysts was determined by rapid recombination of photogenerated electrons and holes. Therefore, enhancing the photocatalytic activity by doping the ZnO nanostructures with a proper mole fraction of Ce^{3+} ions can be attributed to increasing the electron–hole life time.

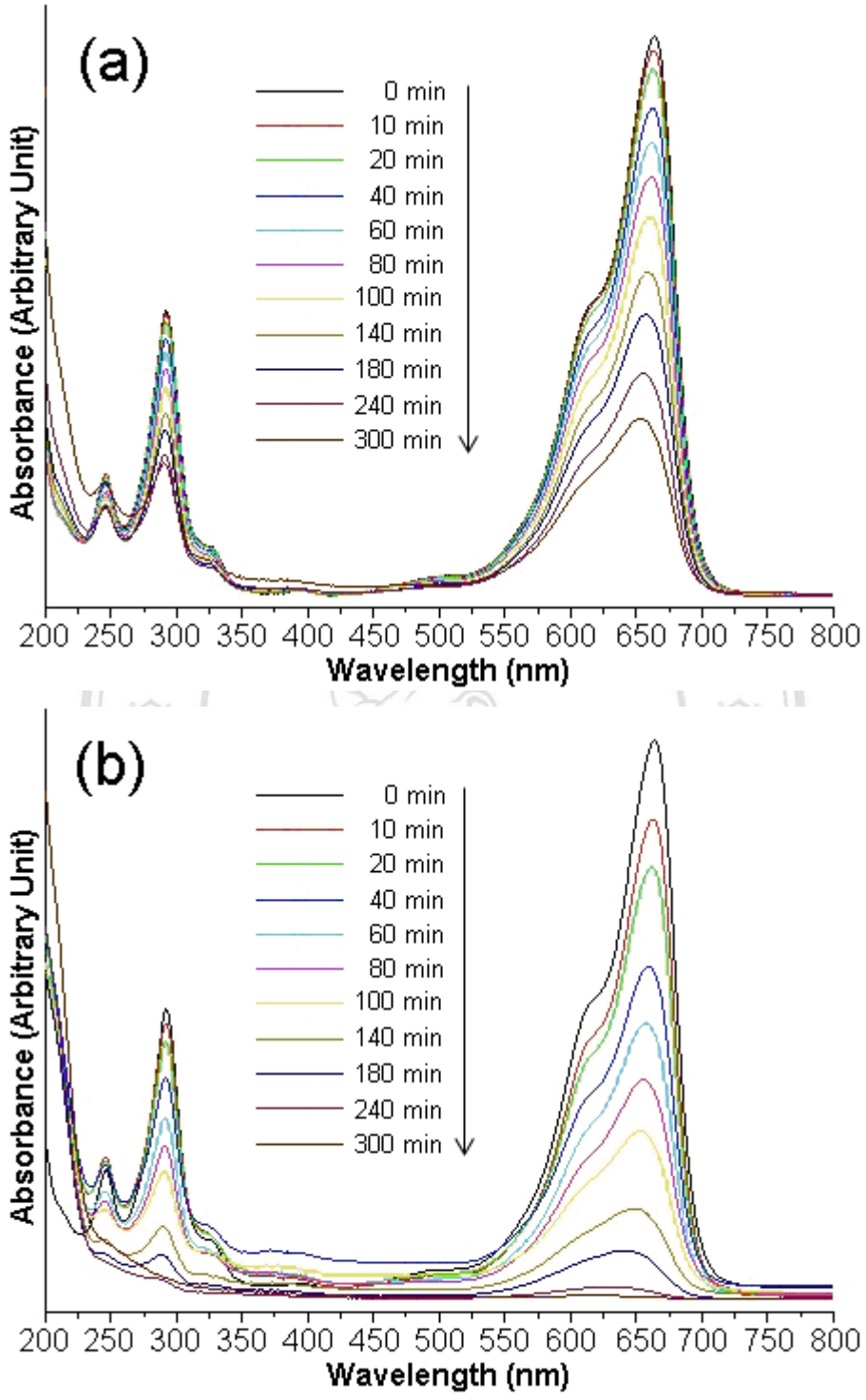

Figure 3.8 UV-visible absorption of MB test during UV light of using (a) ZnO and (b) 3% Ce-doped ZnO.

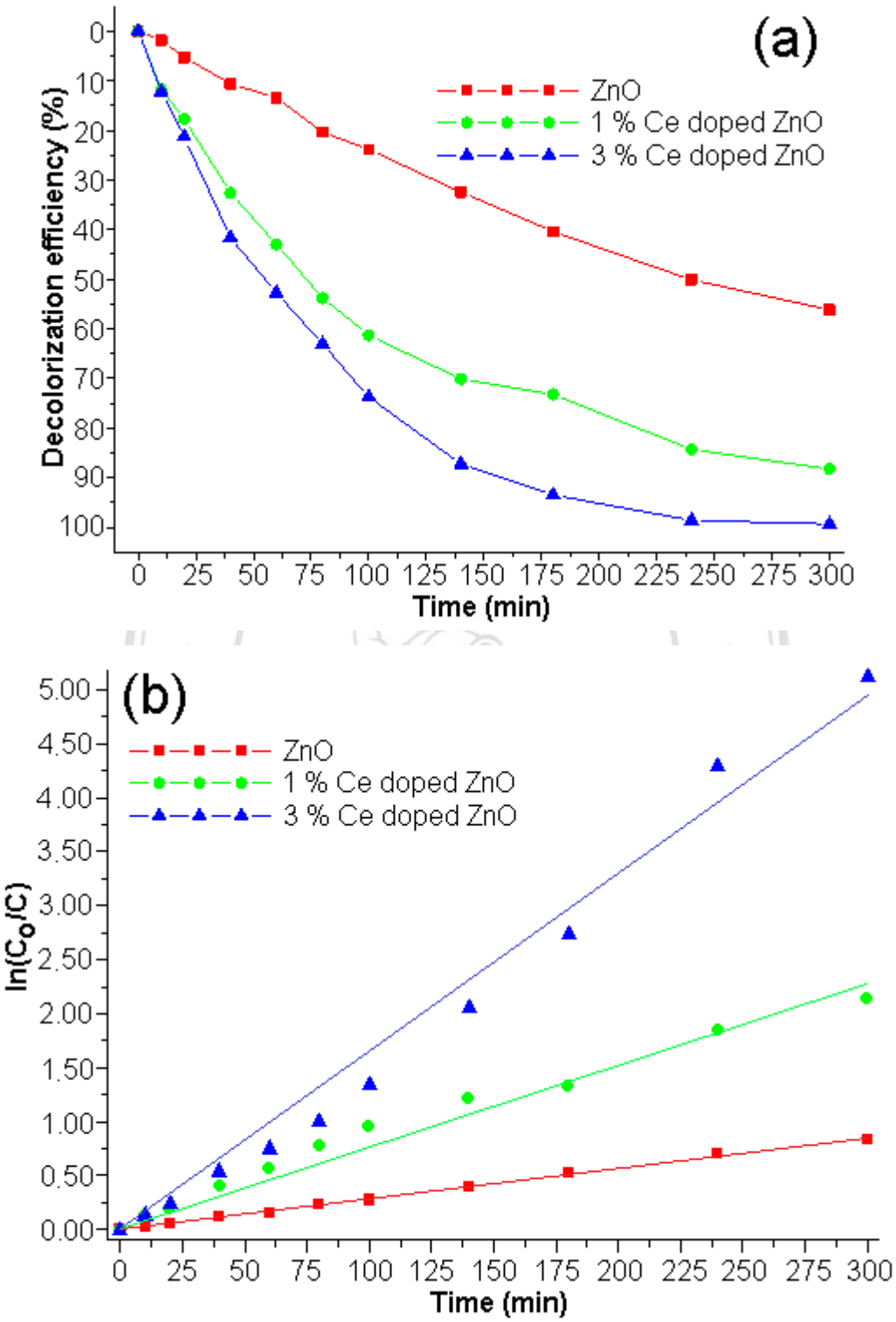

Figure 3.9 (a) Decolorization efficiency and (b) $\ln(C_o/C_t)$ for different lengths of UV irradiation time.

3.2 Ultrasonic-assisted synthesis of Nd-doped ZnO for photocatalysis

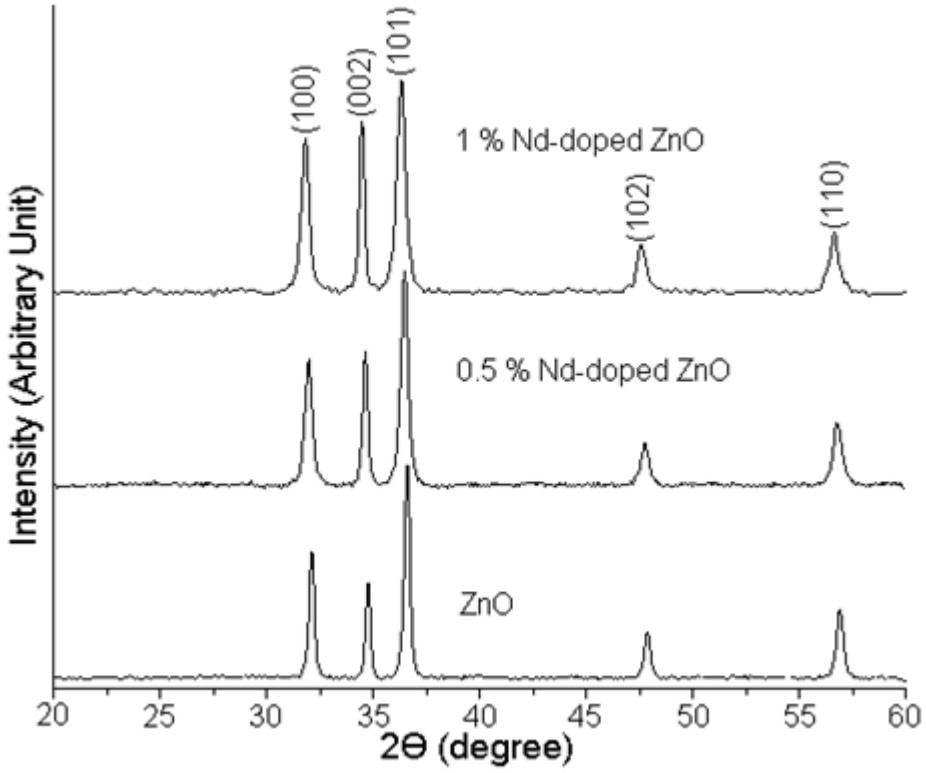

Figure 3.10 XRD patterns of Nd-doped ZnO nanoneedles.

XRD patterns of $Zn_{1-x}Nd_xO$ (x = 0, 0.005 and 0.01) as shown in Figure 3.10 were synthesized by sonochemical radiation for 5 h. The diffraction peaks of undoped ZnO sample appeared at $2\theta = 32.11$, 34.75, 36.59, 47.85 and 56.93 degrees which were identified to the (100), (002), (101), (102) and (110) respectively diffraction planes of wurtzite hexagonal ZnO structure with according to JCPDS No. 36-1451 [34]. However, the XRD patterns of $Zn_{1-x}Nd_xO$ (x = 0, 0.005 and 0.01) were still the same as that of pure wurtzite hexagonal ZnO structure. No Nd_2O_3, $Zn(OH)_2$ and other impurities were detected in these samples. It indicated that the Nd^{3+} ions of the doped ZnO samples were incorporated in the ZnO lattice. It should be noted that the 2θ Bragg's angles of the (100), (002) and (101) peaks for pure ZnO shifted towards the lower ones for 0.5 and 1% Nd-doped ZnO, caused by doping with Nd^{3+} (0.0983 nm radius) into ZnO (0.0740 nm radius for Zn^{2+}) [47] to enlarge lattice parameter of the crystal.

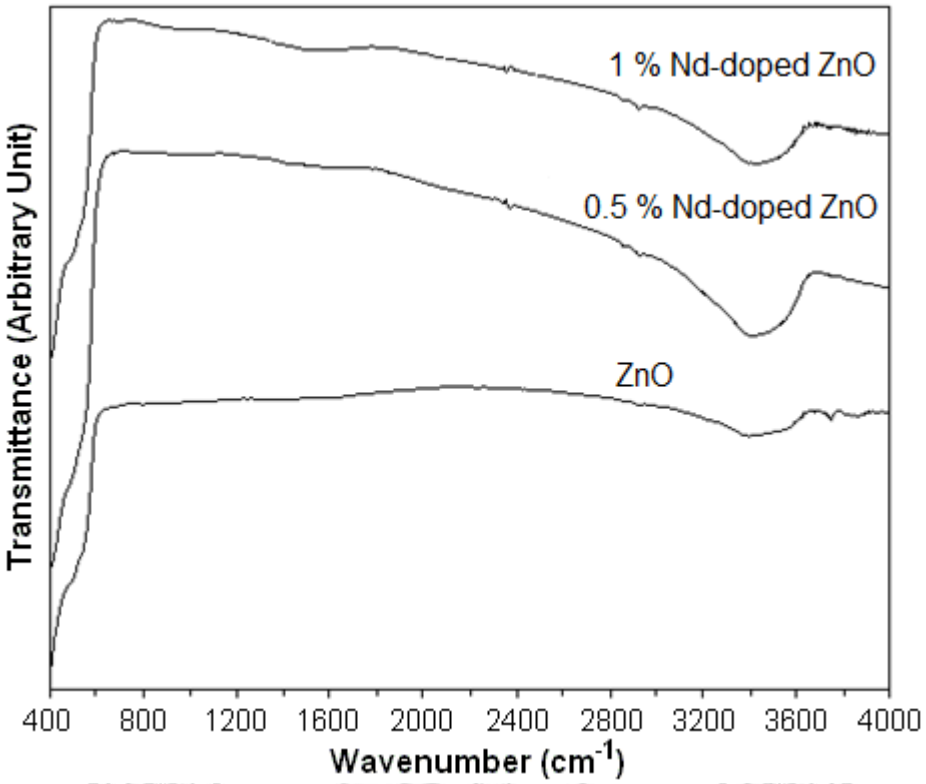

Figure 3.11 FTIR spectra of 0-1% Nd-doped ZnO nanoneedles.

The products were diluted with potassium bromide in the ratio of 1:40 for FTIR analysis. Figure 3.11 shows FTIR spectra of 0 mol%–1.0 mol% Nd-doped ZnO products. The strong absorption bands at 435 cm^{-1} are attributed to the Zn–O stretching vibration of wurtzite hexagonal type ZnO crystal [48], belonging to the oxygen sublattice (E_{2H}) vibration of wurtzite ZnO crystal [48]. The broad absorption bands at 3200–3600 cm^{-1} are the O–H stretching vibration of adsorbed water on ZnO surface [48].

Morphologies of 0–1% Nd-doped ZnO samples were investigated by FE-SEM as shown in Figure 3.12. SEM image of pure ZnO product shows a number of nanoneedles with 50 nm in diameter and 1 μm in length. When Nd was doped to ZnO and the Nd concentration increased from 0.5% to 1%, $Zn_{1-x}Nd_xO$ (x = 0.005 and 0.01) were mostly nanoneedles became 3–4 μm in length.

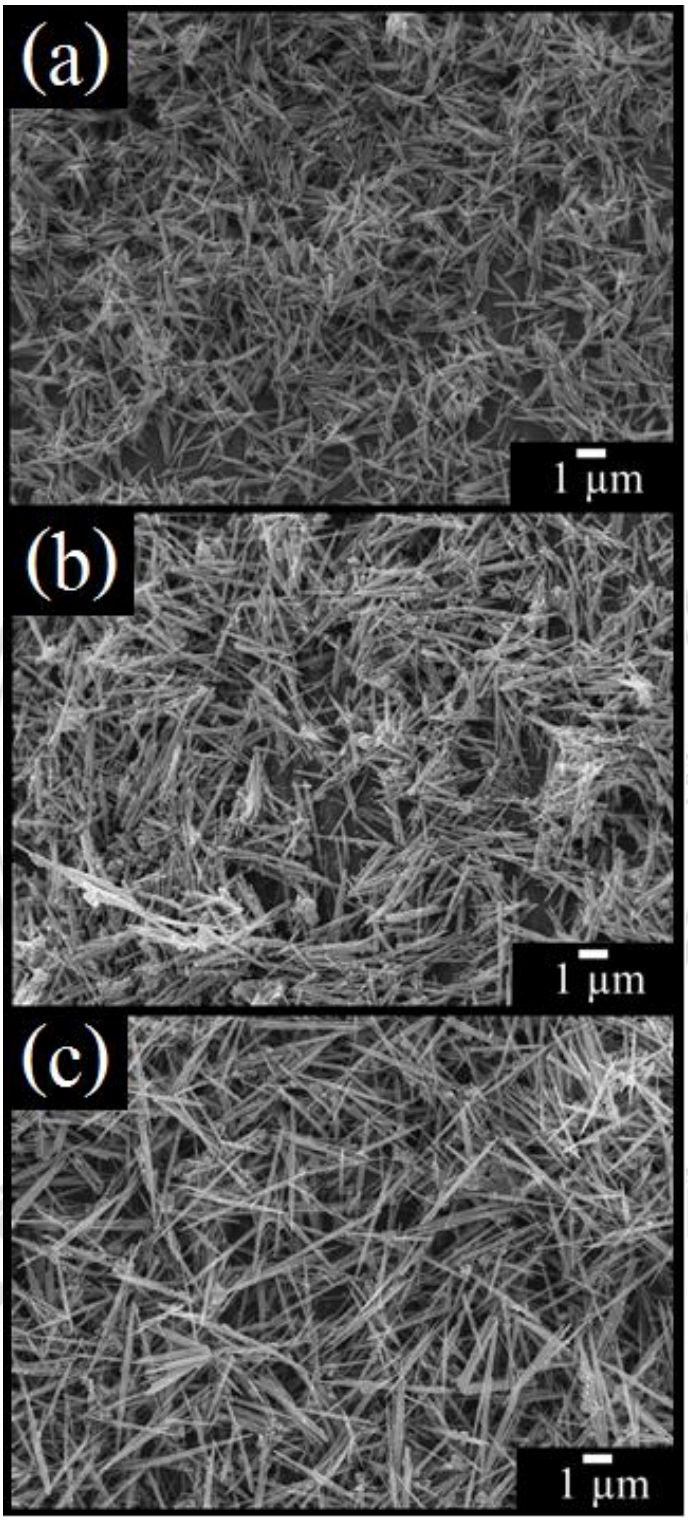

Figure 3.12 SEM images of (a–c) undoped, 0.5% Nd-doped and 1% Nd-doped ZnO, respectively.

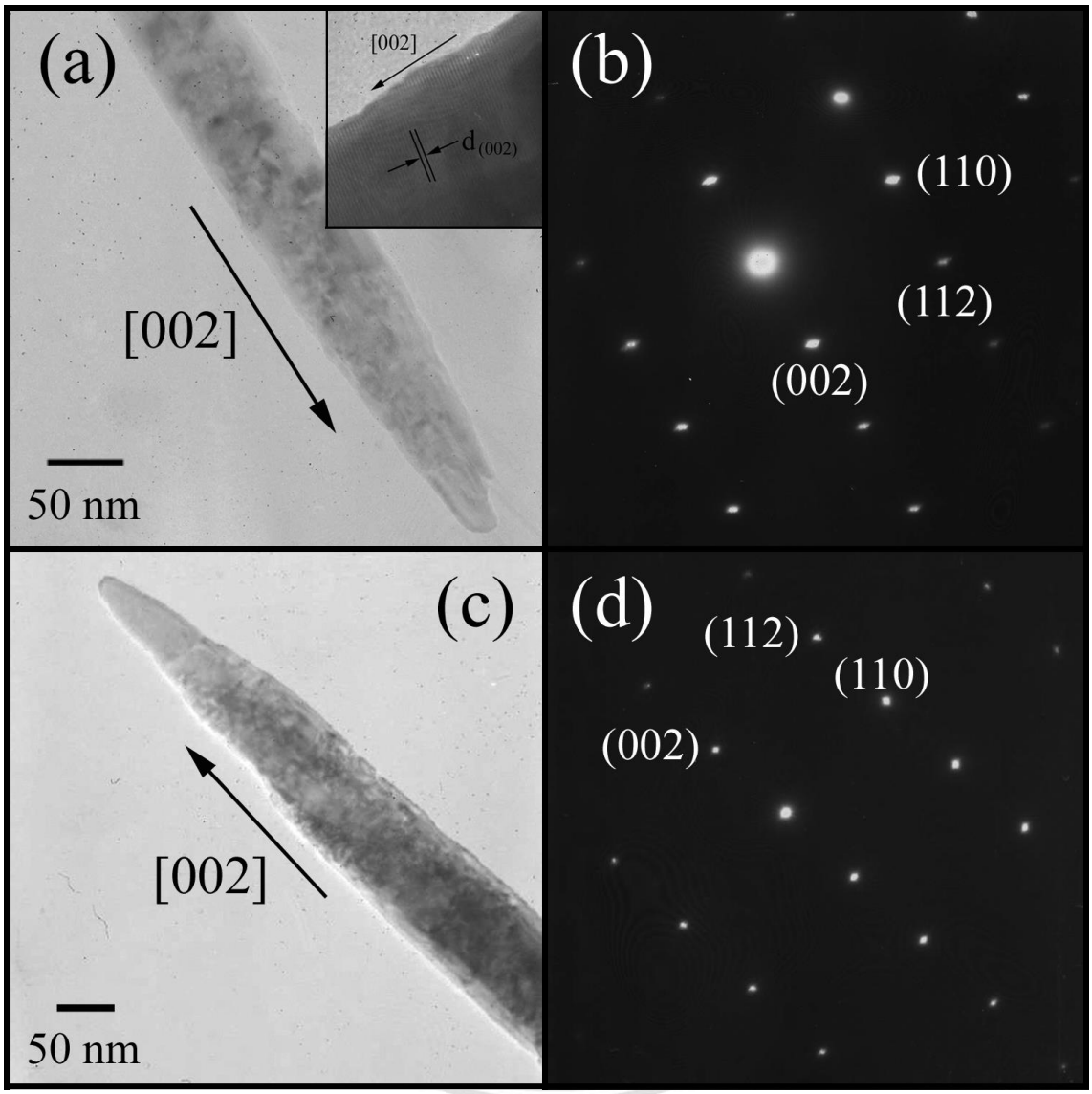

Figure 3.13 TEM, HRTEM and SAED results of (a, b) pure ZnO and (c, d) 1% Nd-doped ZnO.

The detailed morphological characterizations of synthesized ZnO nanoneedles have further analyzed by TEM as shown in Figure 3.13. TEM images (Figure 3.13 (a), (c)) of undoped and Nd-doped samples show similar morphology as nanoneedles with wurtzite single crystalline ZnO specified by their SAED patterns (Figure 3.13 (b), (d)) [34]. An undoped ZnO nanoneedle (Figure 3.13 (a) (inserted)) was rather perfect crystal with no detection of dislocations and stacking faults. It contained a number of stripes with 0.26 nm apart, corresponding to the (002) planes of hcp ZnO. In this analysis, the nanoneedles of undoped and Nd-doped ZnO grew along the [001] direction.

The mechanism of formation of ZnO nanostructures takes the consideration the ionic species formed from water molecules by absorption of ultrasound energy. The reaction steps taking place inside sonochemical bath can be summarised as follows:

$$H_2O \leftrightarrow H^+ + OH^- \quad (3.2)$$

$$NH_4OH \leftrightarrow NH_4^+ + OH^- \quad (3.3)$$

$$Zn(NO_3)_2 \leftrightarrow Zn^{2+} + 2NO_3^- \quad (3.4)$$

$$Zn^{2+} + 4OH^- \leftrightarrow [Zn(OH)_4]^{2-} \quad (3.5)$$

$$2[Zn(OH)_4]^{2-} \leftrightarrow 2ZnO + 4H_2O + O_2 \quad (3.6)$$

Eqs. (3.2)–(3.4) show formation of primary ions which have been formed by dissociation of water, ammonium hydroxide and zinc nitrate. Eqs. (3.5) shows formation of $[Zn(OH)_4]^2$ which further decomposes to give ZnO nanostructures [15]. The preferential growth along the [0001] directions due to the intrinsic anisotropy in its growth rate ν with $\nu[0001] >> \nu[01\bar{1}0] > \nu[000\bar{1}]$. The structure of ZnO single crystal can be described as a number of alternating planes composed of coordinated O^{2-} and Zn^{2+} ions. The oppositely charged ions are made of the positively charged Zn-(0001) and negatively charged O-(0001) polar surfaces. Following the decrease in the concentration of ZnO_2^{2-} monomer due to the initial fast nucleation of ZnO, the absorption of OH^- on the positively charged Zn-(0001) plane would dominate in the competition with ZnO_2^{2-} growth units. Therefore, the superfluous OH^- ions stabilized the surface charge and the structure of Zn-(0001) surfaces to some extent, allowing the fast growth along [0001], leading to the formation of needles-like ZnO structure [39-40].

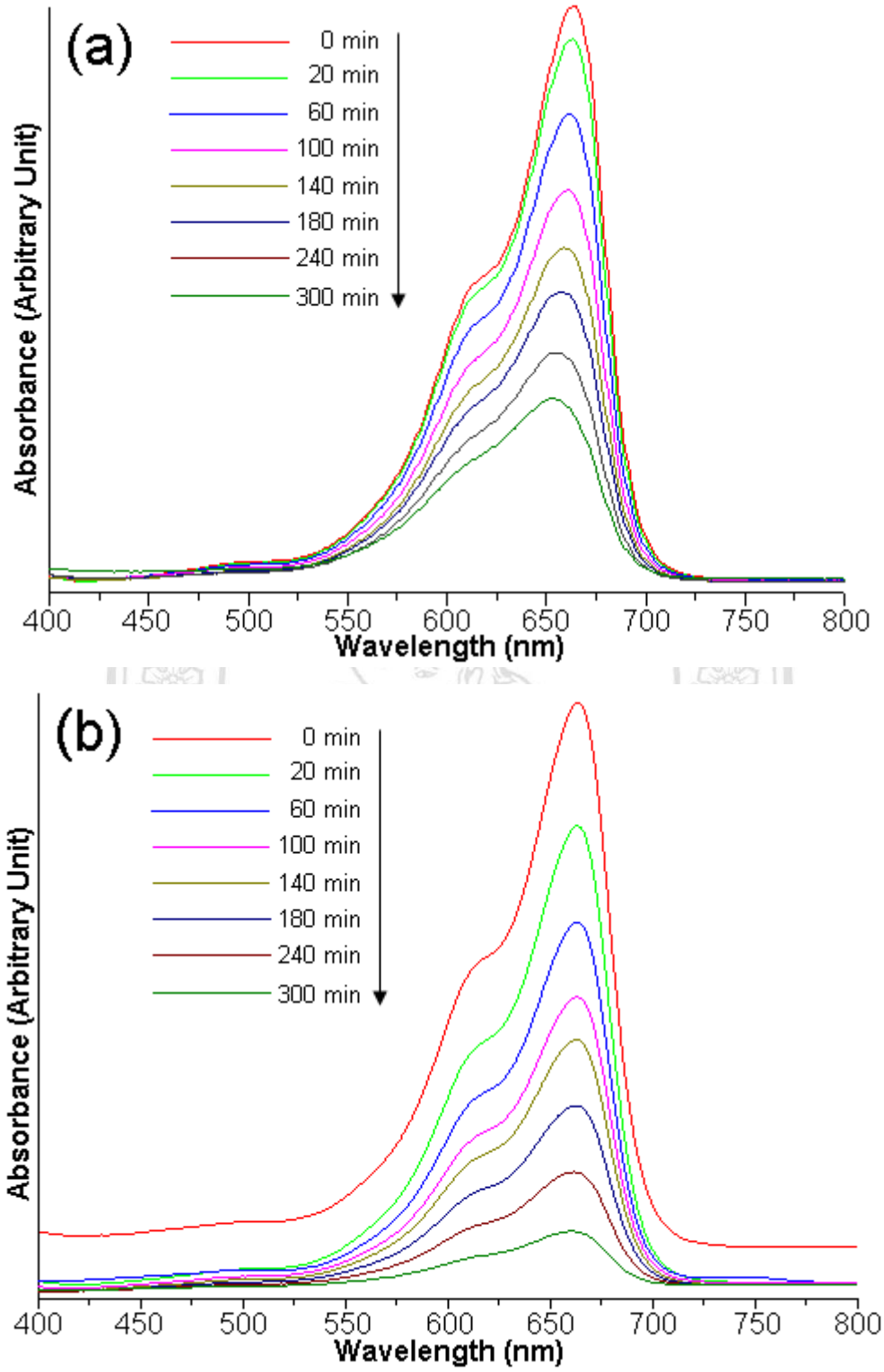

Figure 3.14 UV-visible absorption of MB dissolving in (a) ZnO and (b) 1% Nd-doped ZnO nanoneedles.

Figure 3.14 presents the variation of absorption spectra of aqueous methylene blue (MB) solution containing undoped ZnO and 1% Nd-doped ZnO nanoneedles. The

intensity of the characteristic absorption peak was decreased with the length of irradiation time, indicating the rupture of dye molecules with significant reduction for 300 min. Both undoped and Nd-doped ZnO (Figure 3.15 (a)) can effectively degrade MB molecules, including the photocatalytic enhancement by Nd doping at the highest activity (92%, 300 min) for 1% Nd-doped ZnO. During photocatalysis, Nd^{3+} ions acted as electron scavengers and suppressed electron-hole recombination by promoting the following reactions.

$$Nd^{3+} + e^{-} \rightarrow Nd^{2+} \quad (3.7)$$

$$Nd^{2+} + O_2 \rightarrow Nd^{3+} + \bullet O^{2-} \quad (3.8)$$

The $\bullet O^{2-}$ superoxide ions may initiate a set of reactions as indicated above. The enhancement of Nd was believed to facilitate the photonic absorption of MB by acting as electron acceptor to minimize electron-hole recombination process [49].

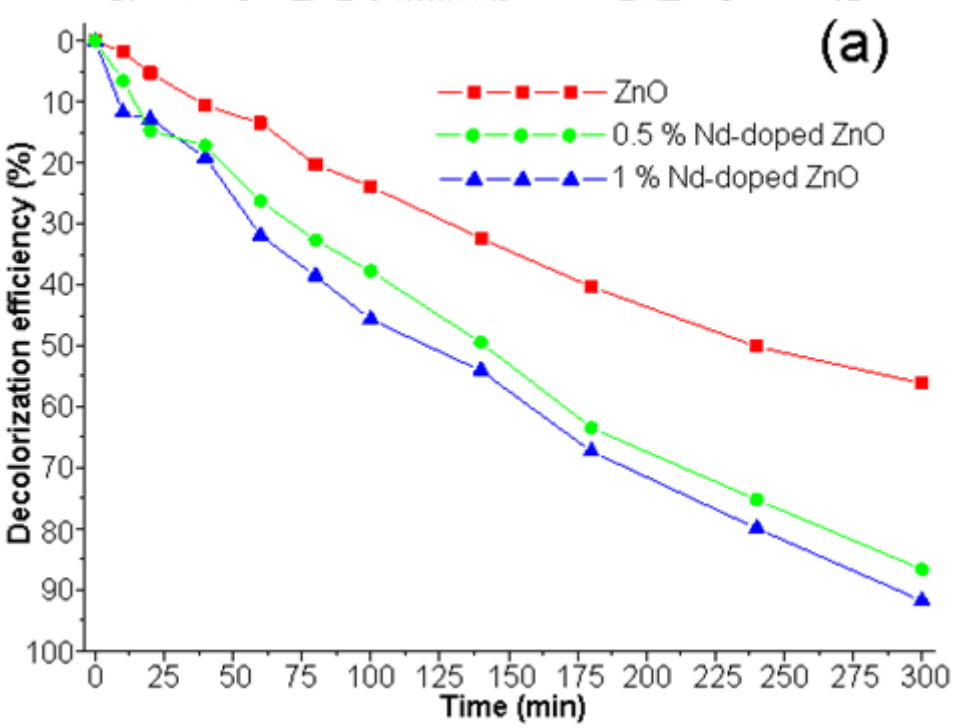

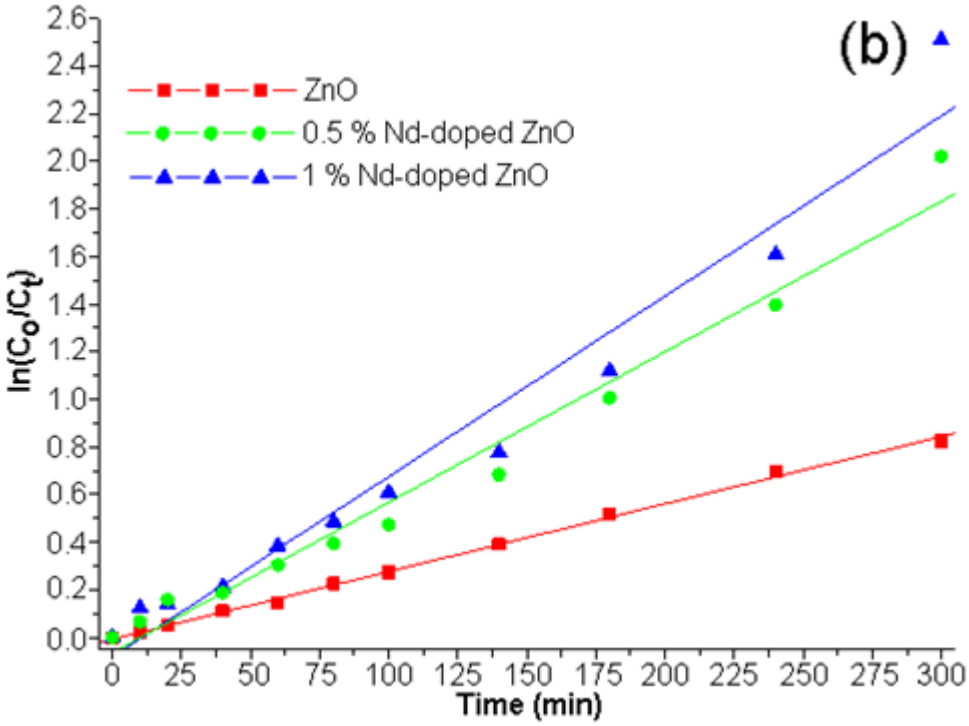

Figure 3.15 (a) Decolorization efficiency and (b) $\ln(C_o/C_t)$ for different lengths of UV irradiation time.

Photocatalytic activity for degradation of MB obeys the pseudo-first-order reaction kinetics with k as the rate constant and t the UV irradiation time [44-46] given by

$$C_t = C_o e^{-kt} \quad (3.9)$$

The plots of $\ln(C_0/C_t)$ versus the irradiation time for the photodegradation of MB (Figure 3.15 (b)) were in straight lines. In this research, the photodegradation followed very well with the pseudo-first order kinetics with $R^2 \rightarrow 1$ (0.9990, 0.9810 and 0.9885 for 0, 0.5 and 1% Nd-doped ZnO, respectively) [30, 50]. For high Nd concentration, the nonlinearity was caused by the increase in surface to volume ratio of Nd-doped ZnO, leading to the increase in exciton formation. This formation could also be increased by longer irradiation time. Their rate constants were respectively 2.9 x 10^{-3}, 6.10 x 10^{-3} and 7.30 x 10^{-3} min^{-1}, revealing the significant effect of Nd-doped ZnO on the photodegradation process. Comparing among the three photocatalysts, their rate constants were increased with the increase in the Nd concentrations. The 1% Nd-doped ZnO showed the best photocatalytic performance with 2.5 times of undoped ZnO.

3.3 Sonochemical synthesis of Dy-doped ZnO nanostructures and their photocatalytic properties

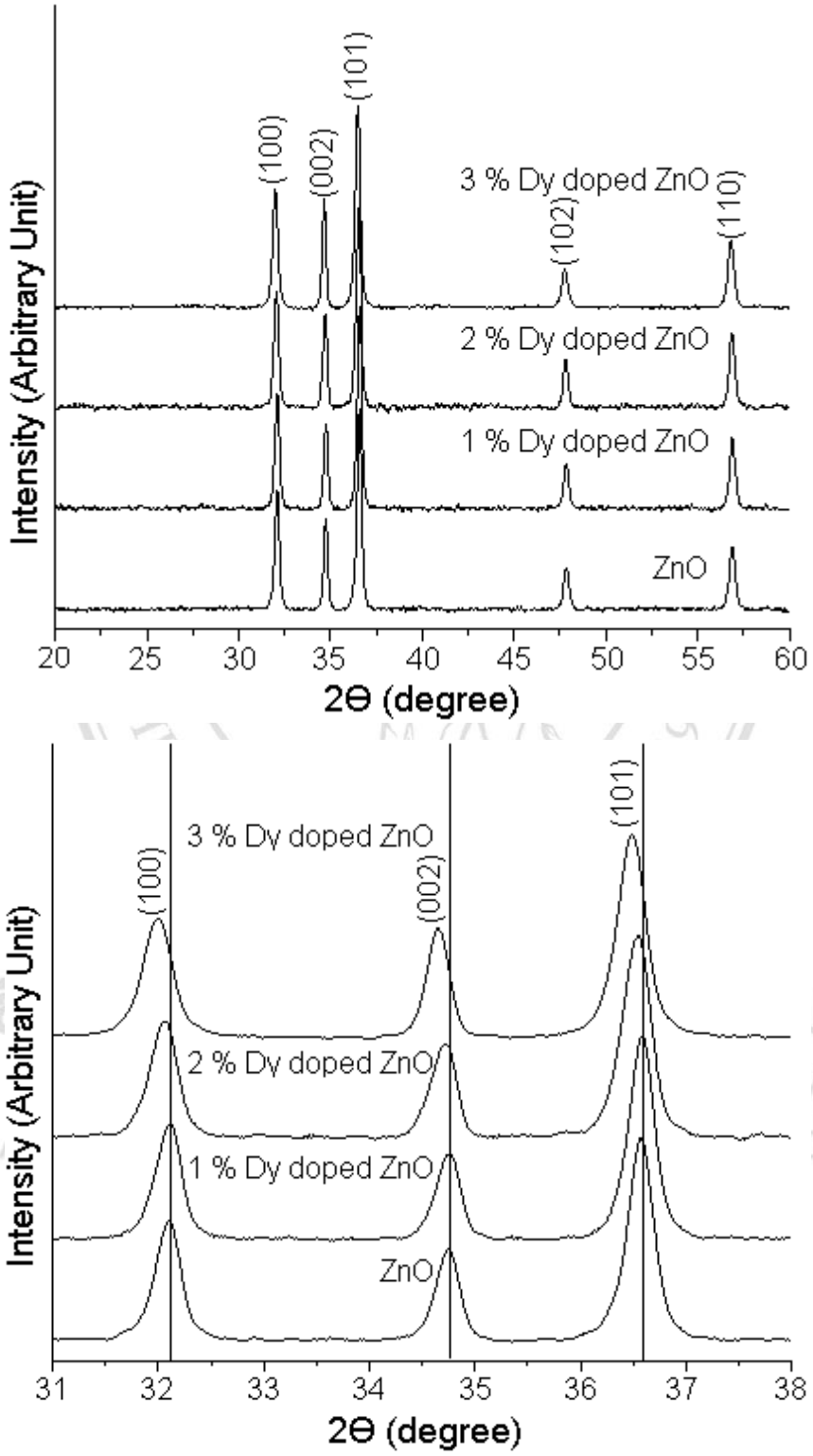

Figure 3.16 XRD patterns of 0–3% Dy-doped ZnO synthesized by sonochemical method over the 2θ range of (a) 20–60 deg and (b) 31–38 deg.

Figure 3.16 (a) shows XRD patterns of the Dy-doped ZnO samples synthesized by ultrasonic solution method. The peaks at 2Θ = 32.11º, 34.75º, 36.57º, 47.87º and 56.89º were detected on pure ZnO sample respectively identified as the (100), (002), (101), (102) and (110) planes of bulk wurtzite hexagonal ZnO structure of the JCPDS file no. 36-1451 [34]. By doping 1–3% Dy in ZnO samples, their XRD patterns still the same as that of pure wurtzite hexagonal ZnO structure. No other peaks corresponding to Dy_2O_3, $Zn(OH)_2$ and other impurities were detected. These indicated that Dy ions of the doped ZnO samples were incorporated in the lattice of ZnO. It should be noted from Figure 3.16 (b) that 2Θ angles of the (100), (002) and (101) planes at 32.11º, 34.75º and 36.57º for pure ZnO was gradually shifted to the lower diffraction values with the increasing in the doping concentrations until reaching at 31.99º, 34.65º and 36.49º by doping with 3% Dy. The phenomenon was explained by the expansion of ZnO lattice caused by the larger radius of Dy^{3+} (0.91 Å) than that of Zn^{2+} (0.74 Å). The increase in lattice parameter and the shift to lower angle of the XRD peaks with increasing in Dy concentration were expected to have the influence on the lattice deformation and strain resulting from Dy dopant [1-3].

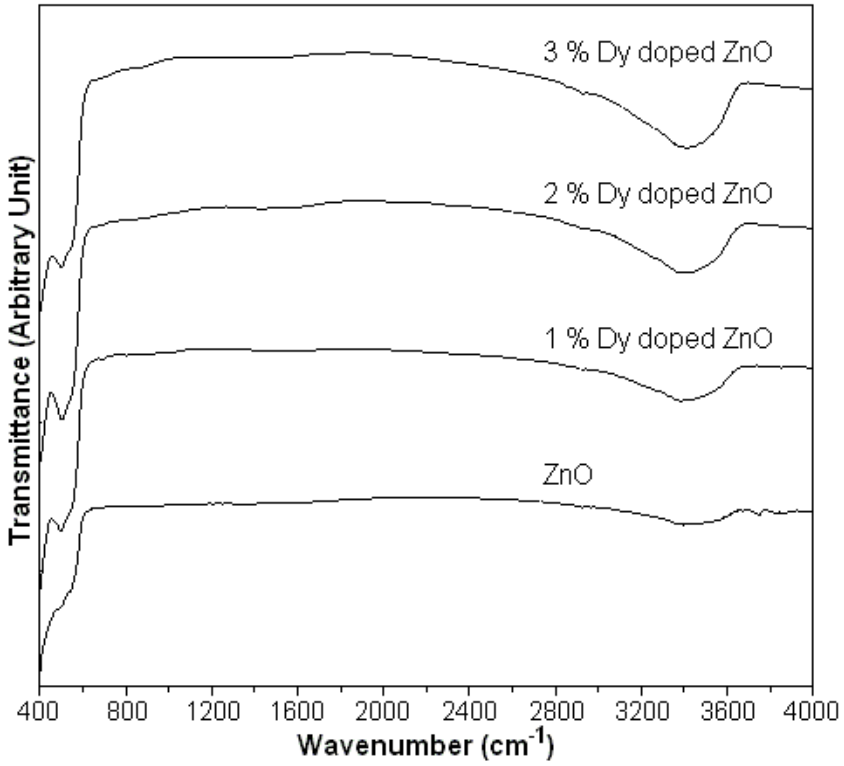

Figure 3.17 FTIR spectra of 0–3% Dy-doped ZnO synthesized by sonochemical method.

FTIR spectra of the 0–3% Dy-doped ZnO samples are shown in Figure 3.17. The samples were diluted with potassium bromide at the ratio of 1:40 and dried at 100 ºC for 24 h to evaporate residual water on surface of the samples before FTIR analysis. The strong absorption bands at 426-565 cm^{-1} were specified as the Zn–O stretching vibration of wurtzite hexagonal structured ZnO crystal [18, 51–53]. Hydroxyl group of rare earth hydroxide ($R(OH)_3$, R = La, Nd, Gd and Dy) showed vibration bands at ~3600 cm^{-1} assigned as the stretching of O–H vibrations [54-56]. In this research, the O–H stretching broad absorption bands were at 3013–3633 cm^{-1} and were increased with the increasing of Dy contents in ZnO. Thus the hydroxyl groups were increased accordingly, due to the expansion of ZnO lattice as the above explanation.

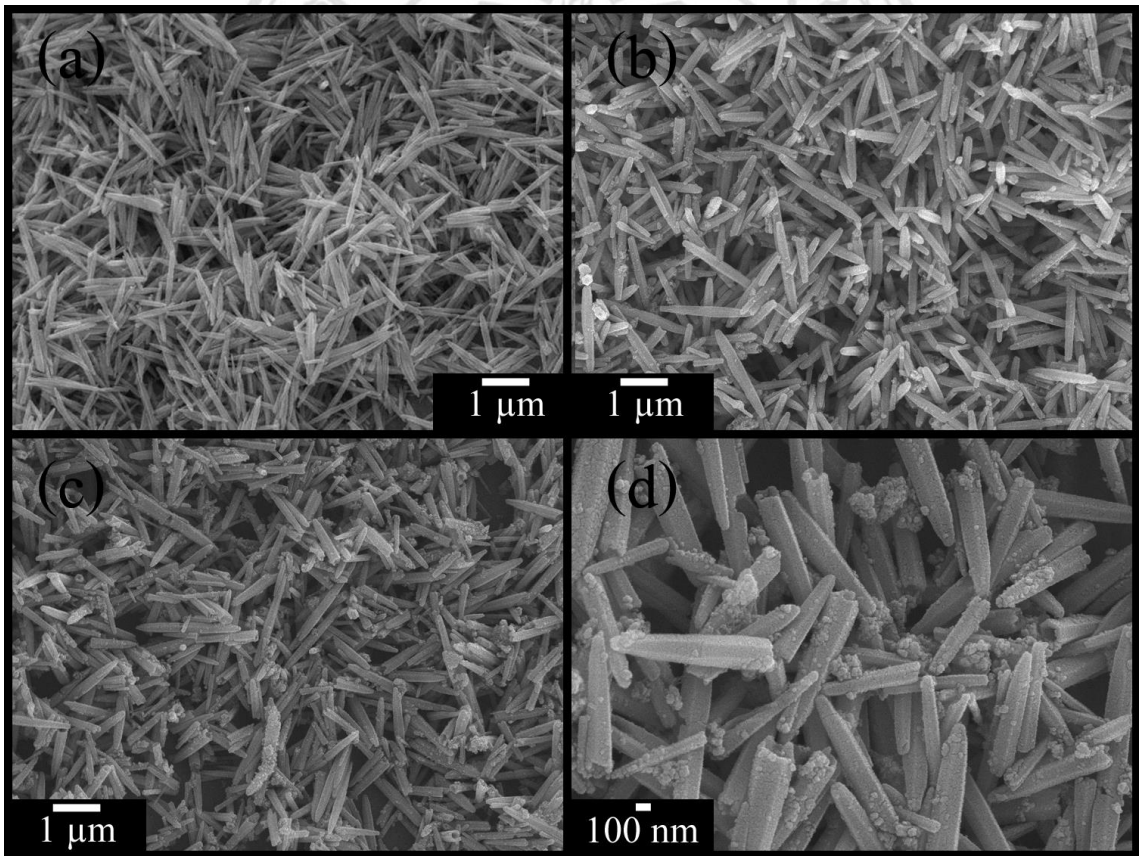

Figure 3.18 SEM images of (a) pure ZnO, (b) 1% Dy-doped ZnO,
(c) 2% Dy-doped ZnO and (d) 3% Dy-doped ZnO.

Figure 3.18 presents typical SEM images of the large area 0–3% Dy-doped ZnO samples synthesized by a sonochemical process with the pH 9.5 at 80 ºC for 5 h. In this research, ZnO was nanorods with 100 nm in diameter and 1–2 μm in length. When Dy

was doped to ZnO and the Dy concentration increased from 1% to 3%, $Zn_{1-x}Dy_xO$ (x = 0.01, 0.02 and 0.03) were mostly nanorods and remained at the same size as pure ZnO. The morphology did not change with further increasing in Dy concentration to 3%. The products were still remaining as nanorods with diameters mainly around 10 nm and the aspect ratio of 2–5.

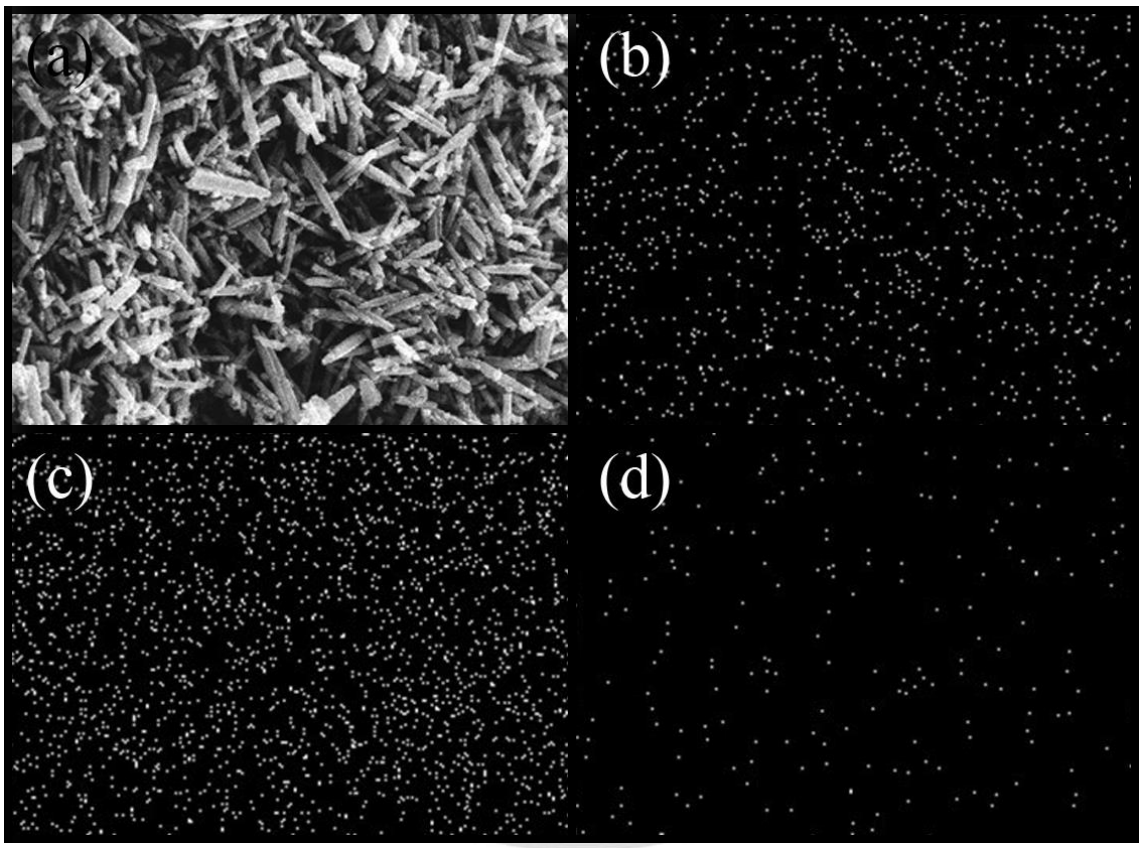

Figure 3.19 (a) SEM image and (b–d) EDX mapping of Zn, O and Dy elements of the as-synthesized 3% Dy-doped ZnO, respectively.

Chemical compositions of the 0–3% Dy-doped ZnO nanorods were determined using energy dispersive X-ray (EDX) spectroscopy. The EDX analysis confirmed the constituent of ZnO nanorods to be the essence of Zn and O although the samples contained traces of Au and Cu due to the sputtered Au covering on surfaces of ZnO nanorods for conductivity increasing and Cu tape as substrates. None of other elemental peaks was detected in EDX analysis for pure ZnO sample. But for the EDX spectra of 1–3% Dy-doped ZnO, the same elements as pure ZnO were detected, including the finding of characteristic X-rays spectrum of Dy. The presence of Dy was 0.92%, 1.95% and 2.93% for 1% Dy-doped ZnO, 2% Dy-doped ZnO and 3% Dy-doped ZnO,

respectively. The EDX mapping of ZnO doped with 3% Dy is shown in Figure 3.19. Dy atoms were found to be very high dispersive across the matrix containing Zn and O.

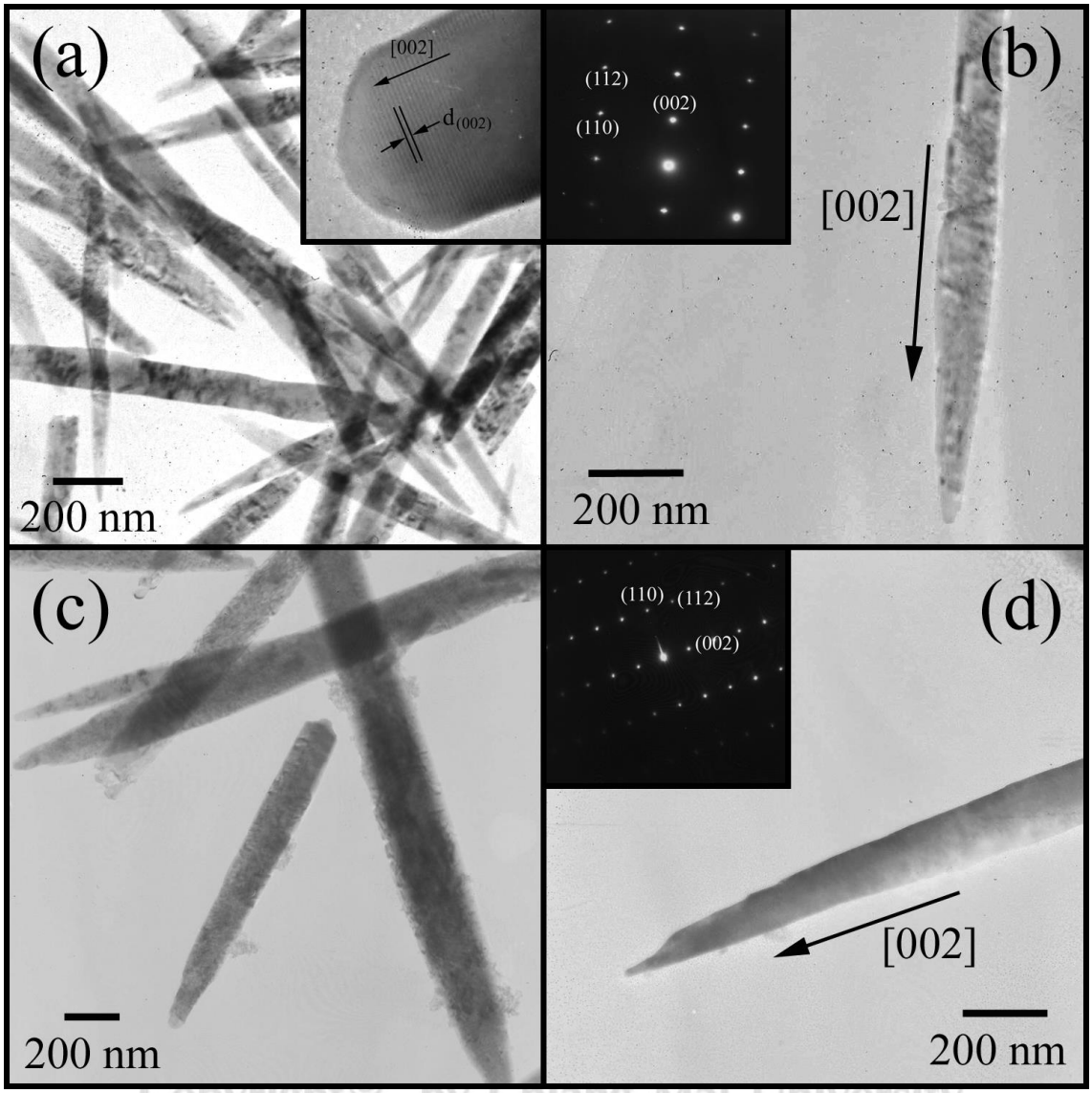

Figure 3.20 TEM images, HRTEM images and SAED patterns of (a, b) ZnO and (c, d) 3% Dy-doped ZnO.

Furthermore, the TEM and HRTEM images, and SAED patterns of pure ZnO and 3% Dy-doped ZnO are shown in Figure 3.20. A typical TEM image of undoped sample presents ZnO nanorods with approximately 20–40 nm in diameter and 200 nm–5 μm in length. HRTEM image of a ZnO nanorod reveals its lattice fringe image of the (002) plane, which indicates the single crystalline ZnO nanorod with the growth direction along the [002] direction. TEM image of 3% Dy-doped ZnO was observed as the

nanorod shaped product which is not much different from that of pure ZnO. The nanorods have wide size distribution with diameters of 20–100 nm and lengths of 40–200 nm. The HRTEM image of an individual 3% Dy-doped ZnO nanorod presents the clear crystal lattice fringe demonstrating that the nanorod was well crystallized. The interplanar distance along the growth axis is 0.260 nm, in consistent with that of the (002) plane of wurtzite structured ZnO. Thus the nanorod was elongated along the c axis. In order to further investigate the product structure, selected area electron diffraction (SAED) was performed on a single nanorod with zone axis of [1-10]. The patterns are in accordance with the single crystalline wurtzite structure.

The experimental results revealed the formation of ZnO nanorods, of which the formation mechanism was considered as ionic species formed from water molecules by absorbing of ultrasonic energy. The reaction steps taking place inside the sonochemical bath were able to be summarized as follows.

$$Zn(NO_3)_2 \leftrightarrow Zn^{2+} + 2NO_3^- \quad (3.10)$$

$$NH_4OH \leftrightarrow NH_4^+ + OH^- \quad (3.11)$$

$$Zn^{2+} + 2OH^- \leftrightarrow Zn(OH)_2 \quad (3.12)$$

$$Zn(OH)_2 \rightarrow ZnO + H_2O \quad (3.13)$$

Primary ions formed by dissociation of zinc nitrate and ammonium hydroxide (Eqs. (3.10) and (3.11)) with subsequent transformation into $Zn(OH)_2$ precipitate (Eqs. (3.12)) [15]. If excess NH_4OH was added, $Zn(OH)_2$ would dissolve in aqueous ammonia to form cationic water-soluble ammine complex. In this research, the precipitate was separated by filtration, and further transformed into ZnO solid during drying (Eqs. (3.13)). The preferential growth along the [0001] direction is due to the intrinsic anisotropy in its growth rate (v) with $v[0001] >> v[01{-}10] > v[000{-}1]$. The structure of ZnO single crystal can be described as a number of alternating planes composed of coordinated O^{2-} and Zn^{2+} ions with oppositely charged ions, which are made of the positively charged Zn-(0001) and negatively charged O-(0001) polar surfaces. Following the decrease in the concentration of ZnO_2^{2-} monomers due to the rapid nucleation of ZnO, the absorption of OH^- on the positively charged Zn-(0001) planes would dominate in the competition with the ZnO_2^{2-} growth units. Thus the OH^- ions stabilized the surface charge of the Zn-(0001) surfaces to some extent, allowing the

rapid growth along the [0001] direction, leading to the formation of nanorod-like structured ZnO [39, 40].

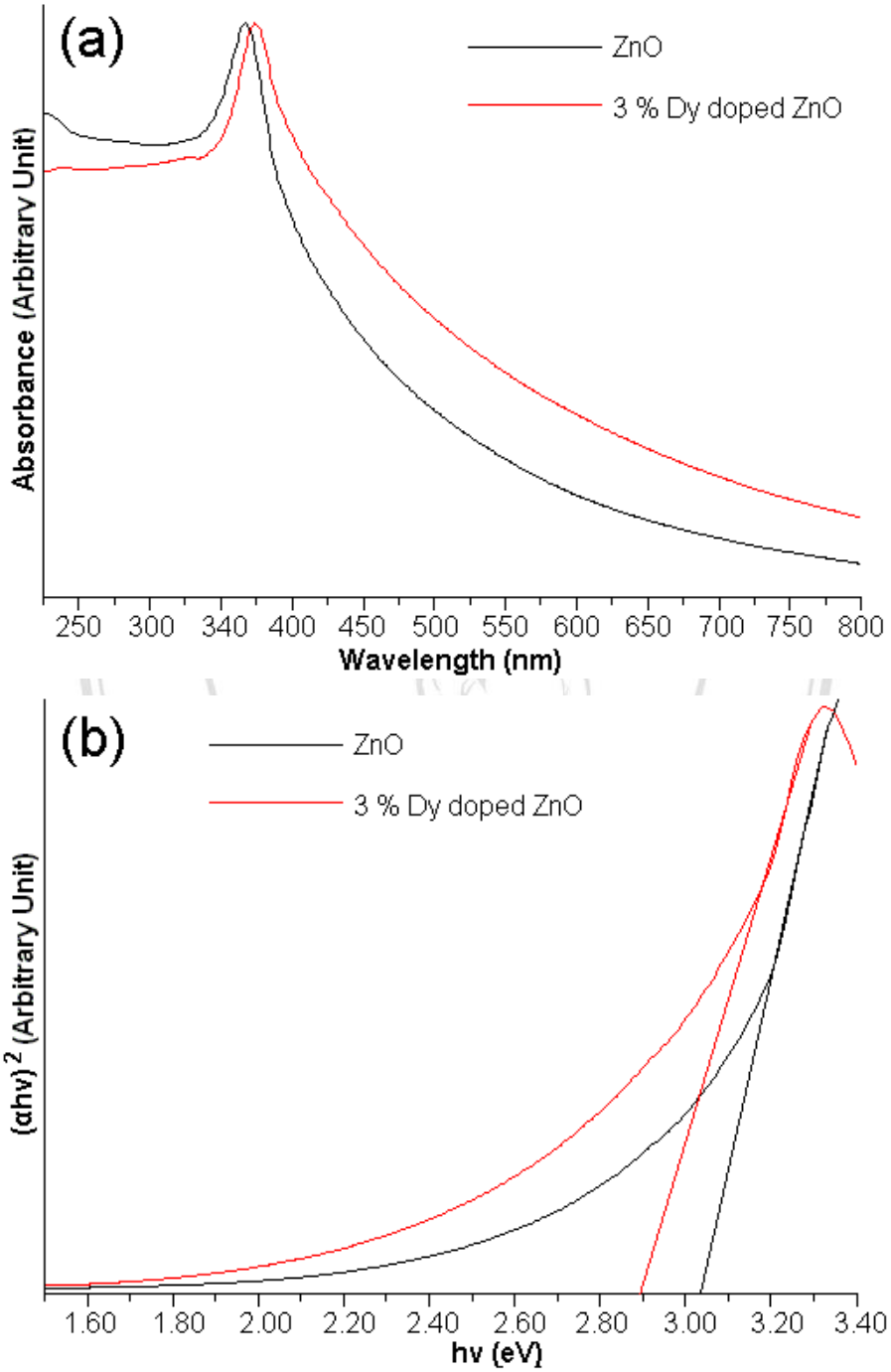

Figure 3.21 (a) UV-visible absorption and (b) the $(\alpha h\nu)^2$ vs hν plots of pure ZnO and 3% Dy-doped ZnO.

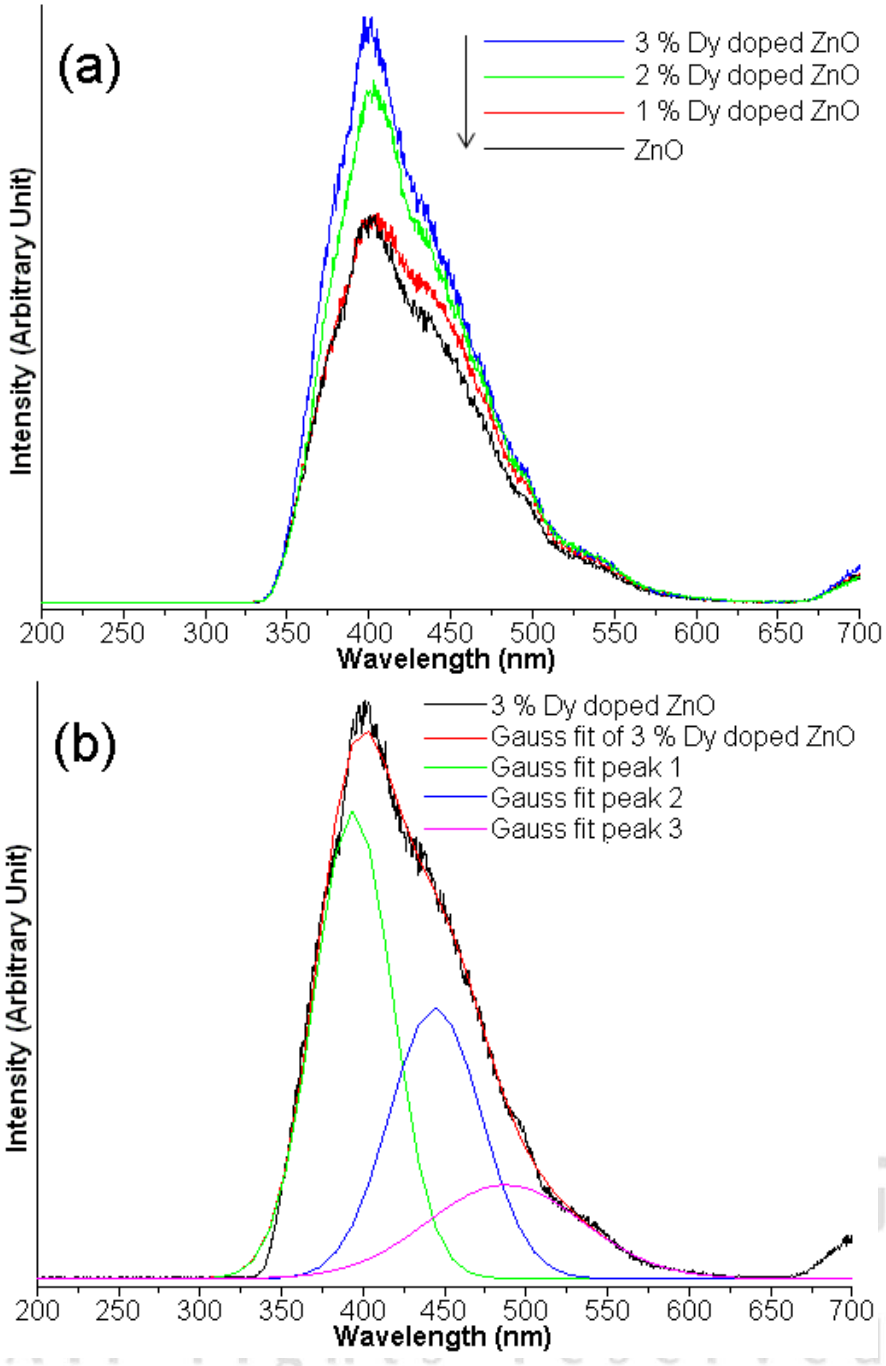

Figure 3.22 (a) PL spectra of 0–3% Dy-doped ZnO and
(b) Gaussian analysis of 3% Dy-doped ZnO.

The optical properties of pure ZnO and 3% Dy-doped ZnO were investigated by UV-visible and photoluminescence spectroscopy as shown in Figure 3.21 and 3.22. The room temperature UV-visible absorption spectrum of the ZnO nanorods shows a peak at 363 nm attributed to the band edge absorption of the pure wurtzite hexagonal ZnO [57]. The band edge absorption began with the wavelength at ~800 nm suggested that more

absorption states or defect energy bands existed in the sample [58]. No other peaks presented in the spectrum which confirms that the as-synthesized product was pure ZnO. Comparing to 3% Dy-doped ZnO, the UV-visible absorption spectrum shows an absorption peak at 373 nm, red shift in comparison with that of bulk ZnO. This red shift can be explained by the formation of shallow level inside the band gap due to impurity atoms residing in the lattice. The photonic energy gap (E_g) of the products was estimated using the Tauc relation

$$\alpha(h\nu) \sim (h\nu - E_g)^{n/2} \tag{3.14}$$

where hν is the photon energy and α the optical absorption coefficient near the fundamental absorption edge. The absorption coefficients were calculated from the optical absorption spectra. The band gap of ZnO was obtained by plotting $(\alpha h\nu)^2$ versus hν in the high-absorption range followed by extrapolating the linear portion of the plots to $(\alpha h\nu)^2 = 0$. Analysis of the present data shows that the plots give linear relations which were fitted with the above equation with n = 1 indicating that direct allowed transitions are responsible for the interband transitions of the products [1, 3, 53]. In this research, pure ZnO and 3% Dy-doped ZnO have the optical energy band gaps of 3.03 eV and 2.89 eV, respectively. E_g of pure ZnO is slightly lower than that of 3.2 eV for bulk ZnO [3, 59].

The photoluminescence (PL) properties for the 0–3% Dy-doped ZnO nanorods were investigated at room temperature using a 318 nm excitation wavelength of Xe lamp as shown in Figure 3.22. A weak near-band-edge-emission in the UV region and a strong broad band deep-level-emission in visible region were observed. By Gaussian analysis, the PL spectrum shows three emissions peaks at 376 nm (48% violet line), 448 nm (33% blue line) and 487 nm (19% green line). The PL peak at 376 nm was due to the recombination of photogenerated holes and electrons with occupying the oxygen vacancies in the ZnO crystalline photocatalyst. The blue emission at 448 nm originated from the irradiative overlap of the electrons transition from the shallow donor level of oxygen vacancies and the defect donor level associated with ionized oxygen vacancies to the valence band. The green broad band around 487 nm is commonly attributed to deep-level or trap-state emission due to vacancies of zinc and oxygen and zinc interstitials in the crystal [16, 61, 62]. The Dy-doped ZnO showed higher in intensity than the undoped ZnO. Their intensities were systematically increased with the increase

in the percent of Dy, which confirmed the dependence of PL intensities with the doping contents. According to literatures, the enhancement of green emission was influenced by the removal of electron captures on surfaces of the nanocrystals or the removal of nonradiative decay channels. The behavior related with the formation of O_{Zn} and V_{Zn} defects associated with oxygen-rich states that were responsible for stronger blue-green emission. Thus the photocatalytic activity of the Dy-doped ZnO can be enhanced by increasing of the Dy concentration [63]. But for ZnO thin film, its photocatalytic activity can be enhanced by increasing in the annealing temperature [64].

There are many reports on photocatalytic properties of ZnO, which is non-toxicity, low cost and synthesis with ease. For the report of the photocatalytic degradation of methylene blue ($C_{16}H_{18}N_3SCl$) by ZnO and TiO_2 photocatalysts, ZnO showed better degradation capability in comparison with TiO_2 under the solar radiation. The result revealed that solar radiation provided a good source of energy to degrade methylene blue (MB) in the presence of ZnO [65]. In addition, zinc oxide as an excellent photocatalytic performance for photodegradation of dyes could be easily prepared in large quantity by direct calcination of zinc acetate dihydrate ($Zn(Ac)_2 \cdot 2H_2O$) [66]. Thus Dy-doped ZnO was used as a photocatalyst in this research. Photocatalytic properties of the samples were evaluated from the absorption intensity of methylene blue (MB) at 664 nm under UV light. Figure 3.23 shows UV-visible spectra of MB in the range of 400–800 nm wavelength after UV irradiation for 0–300 min using pure ZnO and 3% Dy-doped ZnO as photocatalysts. For the same UV irradiation time, the decrease in the absorbance of MB by pure ZnO was slower than that by 3% Dy-doped ZnO. Figure 3.24 (a) shows MB degradation efficiency of the as-synthesized 0–3% Dy-doped ZnO samples. The blank test confirms that MB can only be slightly degraded under UV light without any catalyst [67, 68], indicating that the direct photolysis can be ignored. The Dy-doped ZnO samples exhibited much higher photocatalytic activities than that of the pure ZnO sample. Within 300 min photocatalysis, the decolorization efficiency of ZnO, 1% Dy-doped ZnO, 2% Dy-doped ZnO and 3% Dy-doped ZnO are about 56, 89, 92 and 98%, respectively. The 3% Dy-doped ZnO showed the highest photocatalytic activity. The rapid decrease of the MB concentration was mainly ascribed to the Dy dopant in ZnO. The increase of Dy doping content obviously enhanced the photocatalytic activity.

To investigate the degradation kinetics of MB in solution and quantitatively compare the photocatalytic performances of these samples, the pseudo first-order equation was adopted as Eqs. (3.15):

$$\ln(C_0/C_t) = kt \quad (3.15)$$

where k was the apparent pseudo-first-order rate constant of initial degradation (expressed in units of min^{-1}), C_t and C_0 represents the transient and initial concentrations of MB, respectively [44-46]. As can be seen in Figure 3.24 (b), the order of the k values, which are derived from the plots of $\ln(C_0/C_t)$ versus irradiation time (t), is summarized as follows: 3% Dy-doped ZnO > 2% Dy-doped ZnO > 1% Dy-doped ZnO > ZnO. The rate constant k was calculated from the slope of the $\ln(C_0/C_t)$ versus t, It can be found that the degradation of MB shows apparent pseudo-first-order of kinetics. The rate constant of MB degradation was 1.19×10^{-2}, 7.17×10^{-3}, 5.83×10^{-3} and 2.81×10^{-3} min^{-1} in the 3% Dy-doped ZnO, 2% Dy-doped ZnO, 1% Dy-doped ZnO and ZnO process, respectively. For Dy-doped ZnO, the nonlinearity was caused by the increase in surface to volume ratio of Dy-doped ZnO, leading to the increase in exciton formation. This formation could also be increased by longer irradiation time.

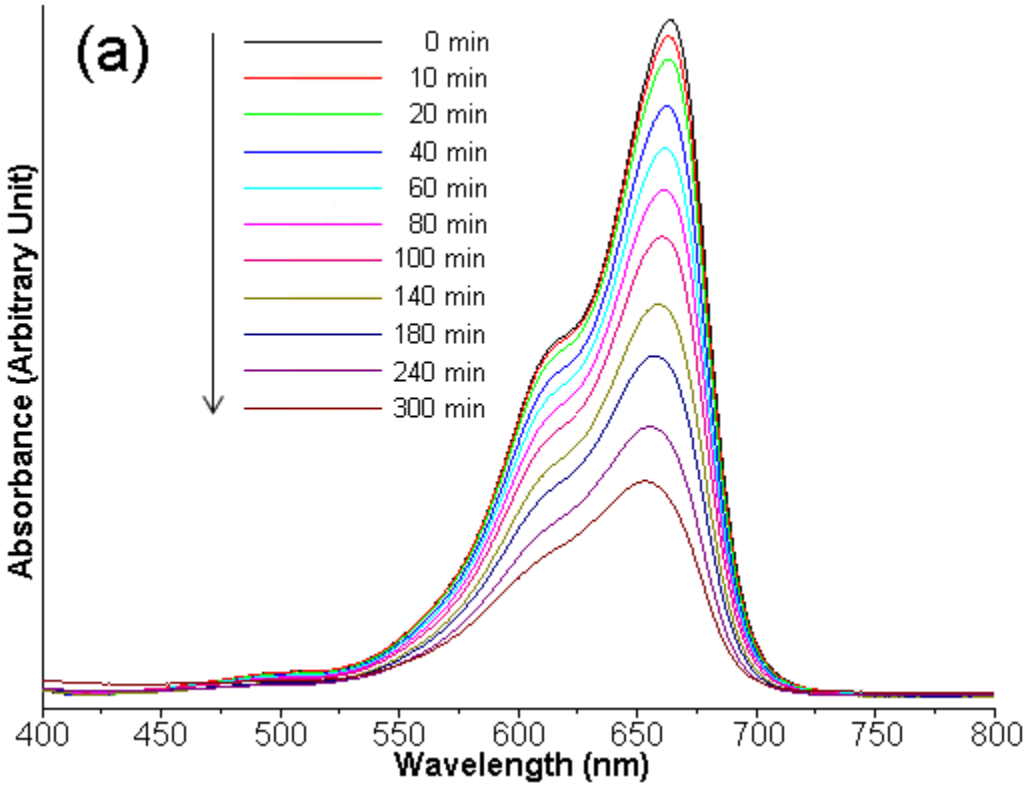

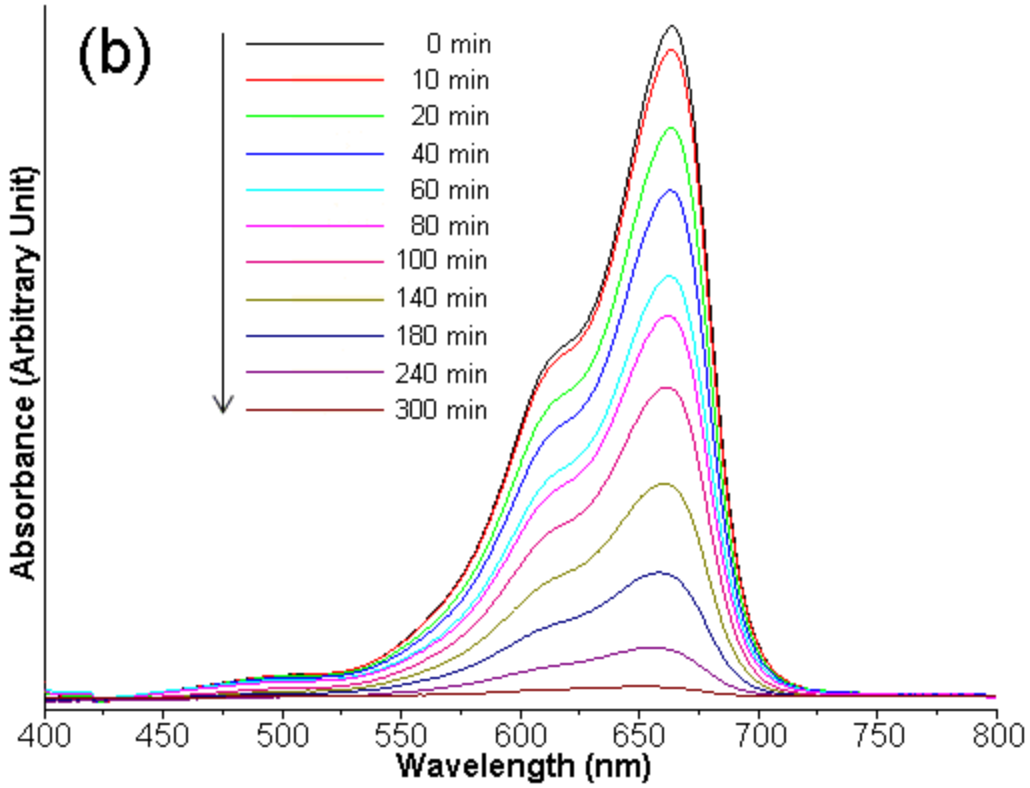

Figure 3.23 UV-visible absorption of MB by UV light irradiation of the solutions containing (a) ZnO and (b) 3% Dy-doped ZnO as the photocatalytic materials.

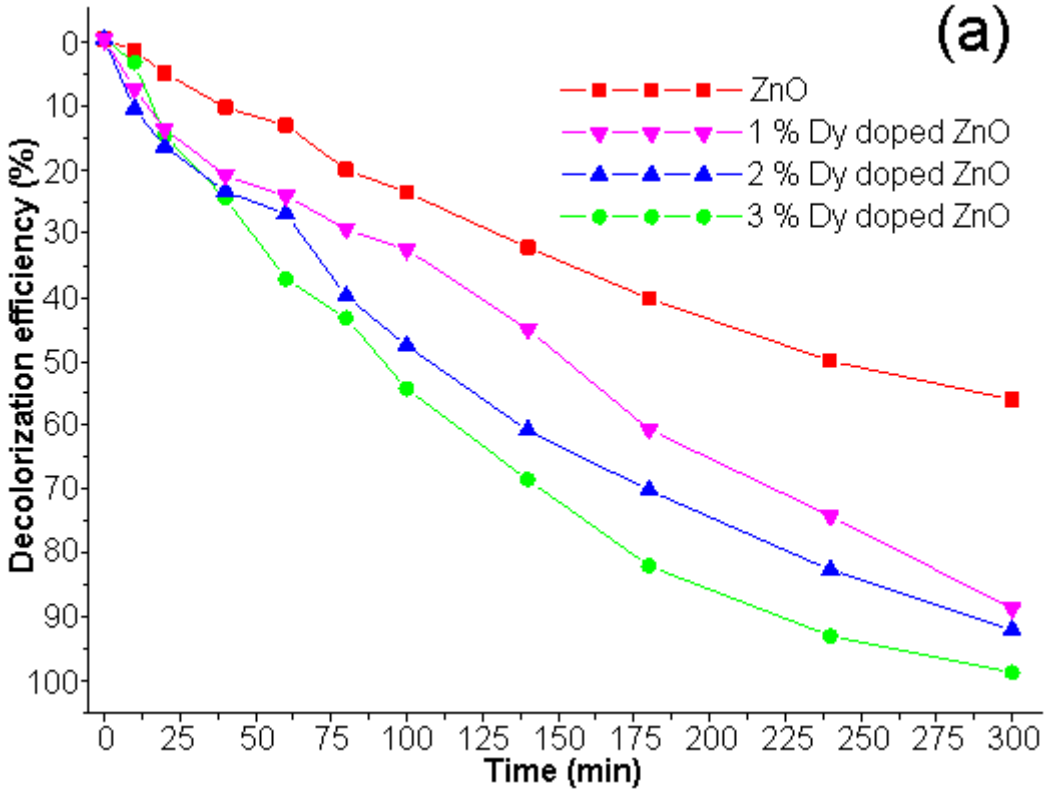

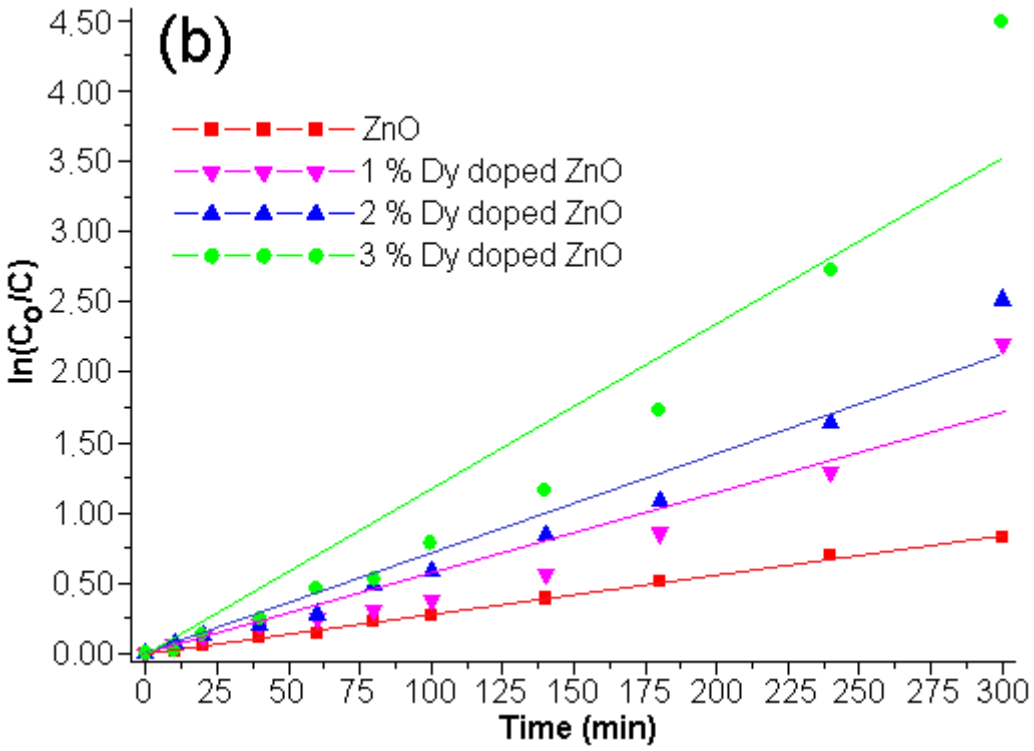

Figure 3.24 (a) Decolorization efficiencies of MB and (b) pseudo-first-order kinetics of 0–3% Dy-doped ZnO during irradiation with UV light.

When nanocrystalline semiconductors are irradiated by photon with energy higher than or equal to the band gap, electrons (e_{vb}^-) in the valence band (VB) will be excited to the conduction band (CB) known as e_{cb}^-, with the simultaneous generation of holes (h_{vb}^+) in the VB. The excited e_{cb}^- and photogenerated h_{vb}^+ are able to recombine, be trapped in metastable surface states or combined with electron donors and electron acceptors adsorbed on the semiconducting surfaces. In other words, the photoelectrons are easily trapped by electron acceptors like adsorbed O_2, whereas the photoinduced holes are easily trapped by negative species, such as OH^- or organic pollutants, to further oxidize organic dyes. Since the oxygen vacancies serve as the electron captures to restrain the recombination of e_{cb}^- and h_{vb}^+. Additionally, the oxygen vacancies are generated as active species on the surfaces of semiconducting materials, which are beneficial to the photodegradation of organic dyes. The corresponding photocatalytic reaction process is able to be formulated as follows.

$$ZnO + h\nu \rightarrow e_{cb}^- + h_{vb}^+ \quad (3.16)$$

$$e_{cb}^- + O_2 \rightarrow \bullet O_2^- \quad (3.17)$$

$$h_{vb}^+ + OH^- \rightarrow \bullet OH \quad (3.18)$$

$$\bullet O_2^- + C_{16}H_{18}N_3SCl \rightarrow \text{oxidation products} \quad (3.19)$$

$$\bullet OH + C_{16}H_{18}N_3SCl \rightarrow \text{oxidation products} \quad (3.20)$$

The good results of photocatalytic activity were obtained by the use of ZnO doped with Nd^{3+} and Ce^{3+}. The transitions of 4f electrons of rare earth lead to the enforcement of the optical adsorption of catalysts and support the separation of photogenerated electron-hole pairs. In case of dysprosium dopant, it can exist as Dy^{3+} and Dy^{4+}. Thus Dy^{3+} may give an electron to O_2 adsorbed on the surface of Dy-doped ZnO to form $\bullet O_2^-$, by transforming into Dy^{4+}, favoring a charged migration to O_2 and an enhancement of the photoreaction rate in comparison with pure ZnO. On the other hand, the Dy^{4+} species may receive photogenerated electrons in conduction band of ZnO to form Dy^{3+}. These reactions are responsible for the enhanced photoactivity of ZnO along with the photonic absorption wavelength in UV region, which is similar to that observed by using other transition metal species. In the end, Dy dopant can effectively slow down the recombination rate of the photogenerated electron-hole pairs and enhance interfacial charged transfer efficiency. The process improves the photocatalytic activity of ZnO, in the same manner as the transfer of photogenerated electron from conduction band to d orbitals of transition metal doped ZnO [22, 69]. Due to the photocatalytic process, MB molecules were degraded by transforming into the colorless species of CO_2, NH_4^+, NO_3^-, SO_4^{2-}, Cl^- and H_2O [23, 70]. It should be noted that the electron-hole recombination process was effective at 376, 448 and 487 nm wavelengths. At higher wavelength, the recombination was ineffective. Thus the separation of photogenerated electron-hole pairs at 664 nm wavelength was enhanced by the Dy dopant in ZnO, and the separation efficiency of 3% Dy-doped ZnO was the highest. The 3% Dy-doped ZnO lattice was the most open texture as the above explanation which also facilitated the photocatalytic process.

3.4 Synthesis and characterization of highly efficient Gd-doped ZnO photocatalyst irradiated with ultraviolet and visible radiations

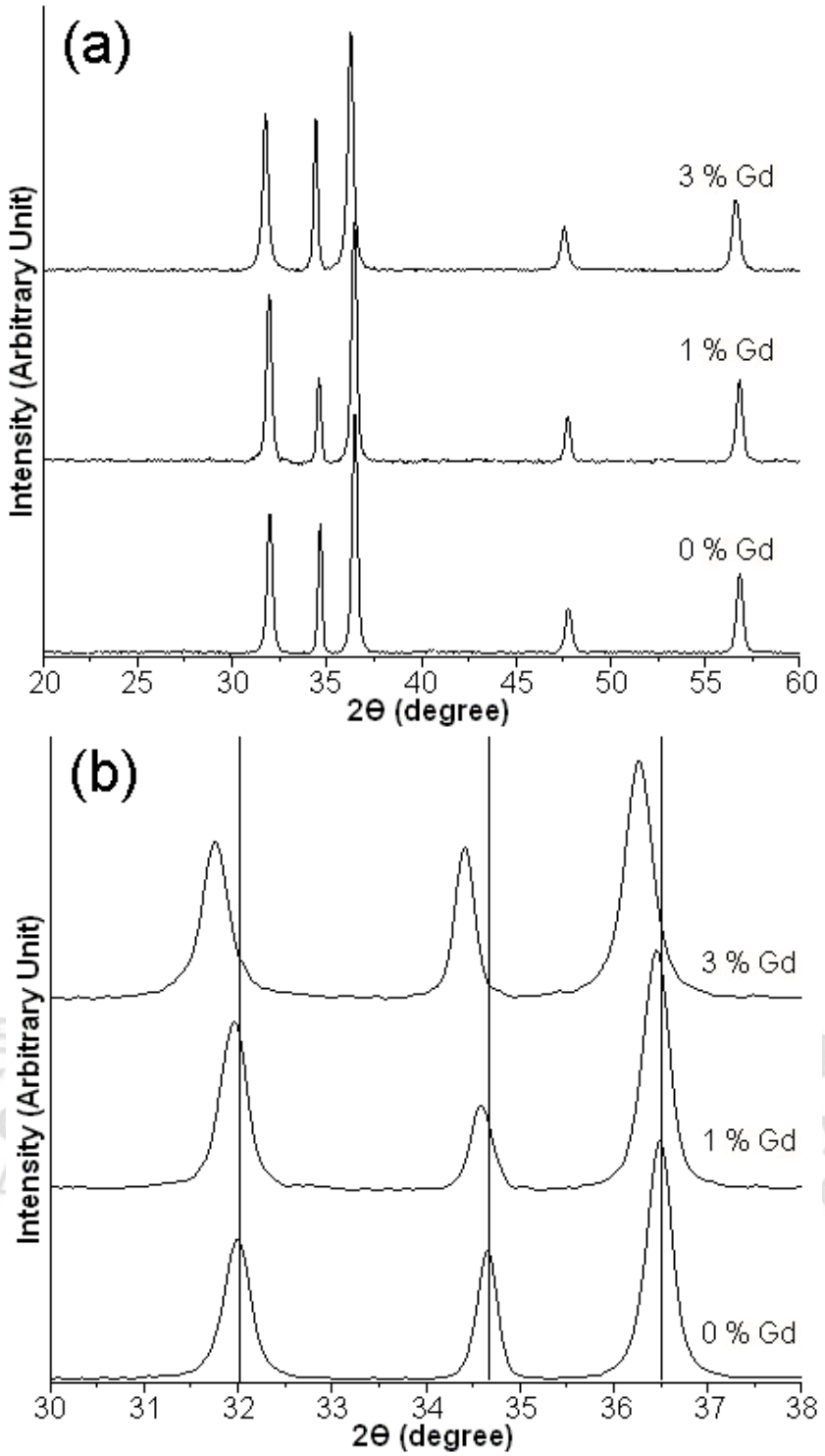

Figure 3.25 XRD patterns of undoped ZnO, and of 1 mol% Gd and 3 mol% Gd-doped ZnO synthesized by sonochemical method over the 2θ range of (a) 20–60 deg and (b) 30–38 deg.

Figure 3.25 (a) shows XRD patterns of the as-synthesized Gd-free, 1 mol% Gd and 3 mol% Gd-doped ZnO products. XRD pattern of undoped ZnO shows five peaks at 2θ = 32.11º, 34.75º, 36.57º, 47.87º and 56.89º and were respectively indexed to the (100), (002), (101), (102) and (110) planes of hexagonal wurtzite structure (JCPDS file no. 36-1451 [34]). By doping 1 mol% and 3 mol% Gd in ZnO, their XRD patterns are still the same as that of pure wurtzite ZnO structure, without detection of other peaks corresponding to gadolinium oxide and other impurities. Gd-doped ZnO was unable to be synthesized by increasing the Gd dopant to 4 mol%. Possibly, the Gd dopant was excessive. To confirm the possible substitution of Zn ions by Gd^{3+} ions in Gd-doped ZnO, the 2θ of the (100), (002) and (101) peaks at 32.11º, 34.75º and 36.57º for pure ZnO phase were gradually shifted to the lower diffraction angles with the increasing in the Gd^{3+} concentration until reaching at 31.99º, 34.65º and 36.49º by doping with 3 mol% Gd (Figure 3.25 (b)). These indicated the partial substitution of Gd in the crystalline ZnO structure. Based on the hexagonal structure, the lattice parameters of ZnO at different contents of Gd were determined using the (3.21) and (3.22) equations [71]

$$\frac{1}{d_{hkl}^2} = \frac{4}{3}\left(\frac{h^2 + hk + k^2}{a^2}\right) + \frac{l^2}{c^2} \quad (3.21)$$

$$\lambda = 2d_{(hkl)}\sin\theta \quad (3.22)$$

, where (hkl) are the Miller indices, d_{hkl} are the interplanar spaces for the (hkl) planes at 2θ Bragg's angles, λ is the X-ray wavelength of Cu K_α (1.54056 Å), and a and c are the lattice constants of the ZnO and Gd-doped ZnO. A slight increase of ZnO lattice parameters resulted from Gd doping was also observed as the results shown in Table 3.1. The phenomenon was explained by the expansion of ZnO lattice caused by the possible substitution of Gd^{3+} (radius 0.938 Å) [72] into Zn^{2+} (radius 0.74 Å) lattice [33, 73] of the ZnO crystal.

The grain size (D) was calculated from the diffraction peaks of ZnO and Gd-doped ZnO using the Debye Scherrer's formula [71] as follows

$$D = \frac{0.89\lambda}{\beta\cos\theta} \quad (3.23)$$

, where λ is an X-ray wavelength (1.54056 Å), β is the full width at half maximum (FWHM) of the diffraction peak and θ is the Bragg's diffraction angle. The calculated average grain size of the samples is summarized in Table 3.1.

Table 3.1 Average grain size and lattice parameter of undoped ZnO, 1 mol% Gd-doped ZnO and 3 mol% Gd-doped ZnO.

Sample	Average grain size (nm)	Lattice parameter (Å)	
		a	c
ZnO	23	3.2332	5.1733
1 % Gd doped ZnO	26	3.2343	5.1823
3 % Gd doped ZnO	25	3.2499	5.2086

Wurtzite-type ZnO belongs to the space group C^4_{6v} with two formula units in the primitive cell. At the central point of the Brillouin zone, group theory predicts the existence of the following phonon modes

$$\Gamma = 2A_1 + 2B_1 + 2E_1 + 2E_2$$

Among these modes, there are acoustic modes with $\Gamma_{aco} = A_1 + E_1$ and optical modes with $\Gamma_{opt} = A_1 + 2B_1 + E_1 + 2E_2$. For optical modes, B_1 modes are Raman silent. Both A_1 and E_1 are polar and are split into transverse (TO) and longitudinal optical (LO) phonons. A nonpolar phonon mode with symmetry E_2 has two frequencies: E_{2H} associated with oxygen atoms and E_{2L} associated with Zn sublattice. Among the optical modes, A_1, E_1 and E_2 are Raman active [73-75].

Figure 3.26 shows Raman spectra of the as-prepared ZnO and 3 mol% Gd-doped ZnO using 514 nm wavelength of an argon green laser. Five Raman modes are observed at 201, 332, 384, 438 and 578 cm^{-1}. The peak at 332 cm^{-1} is assigned to the second-order Raman spectrum arising from zone boundary phonons E_{2H}–E_{2L} [33, 75, 76]. The peak located at 438 cm^{-1} is attributed to the ZnO nonpolar optical phonons of E_{2H} mode, one of the characteristic peaks of wurtzite ZnO [33, 73-76]. The peak at 384 is associated with the A_1(TO) which is also the first-order optical mode of wurtzite ZnO [33, 73, 76]. The small peak observed at 201 cm^{-1} is attributed to E_{2L} which is the second-order feature caused by multiphonon processes [76]. The Raman peaks located around at 500–

600 cm^{-1} are attributed to the intrinsic lattice defects of O-vacancy, Zn-interstitial and their complexes. Comparing with the Gd-doped ZnO samples, the peak located around 578 cm^{-1} shifted to higher wavenumber, due to the change of free carrier concentration in the sample [75].

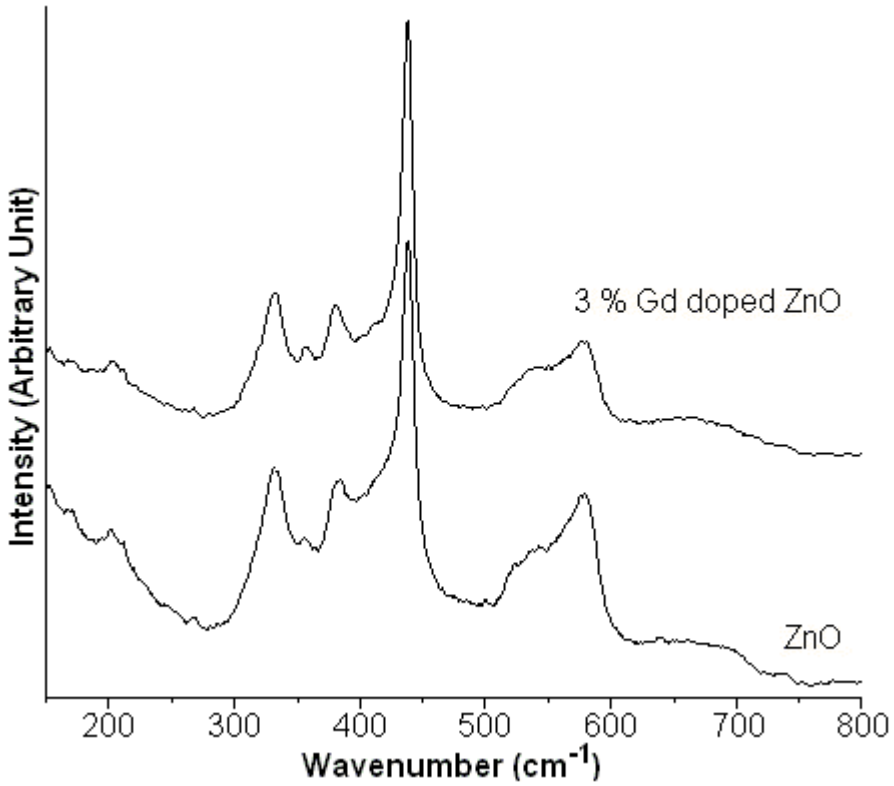

Figure 3.26 Raman spectra of the undoped ZnO and 3 mol% Gd-doped ZnO synthesized by sonochemical method.

The typical morphologies of the as-synthesized pure ZnO and Gd-doped ZnO products are shown in Figure 3.27. The FE-SEM images indicated that the as-synthesized products were nanorod shape, having diameter and length in the range of 100 nm and 1–2 μm. The growth of ZnO was independent of Gd doping ions. The morphology remained unchange with further increasing in the Gd concentration to 3 mol%. Molar content of the doping agent in comparison with ZnO source was too low to alter the morphology. The 3 mol% Gd-doped ZnO remained as nanorods with diameters mainly around 10 nm and the aspect ratio of 2–5. The average diameter of the as-synthesized Gd-doped ZnO was smaller than that of the pure ZnO nanorods. The elemental analysis on the as-synthesized products was identified by EDX, and found to consist of Zn, Gd and O, indicating the dopant in Gd doped ZnO product exist as elemental Gd.

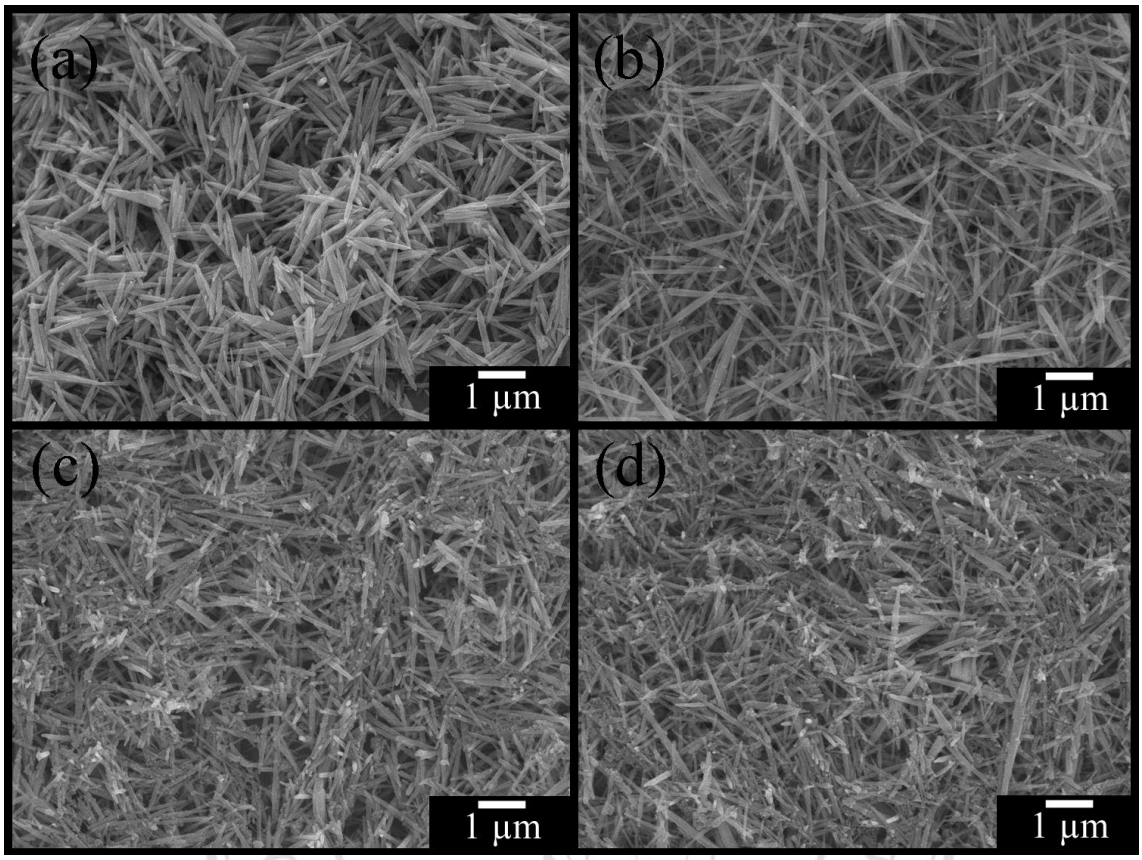

Figure 3.27 SEM images of (a) undoped ZnO, (b) 1 mol% Gd-doped ZnO, (c) 2 mol% Gd-doped ZnO and (d) 3 mol% Gd-doped ZnO.

For detailed microstructure characteristics of ZnO and Gd-doped ZnO, TEM and SAED analyses were done as the results indicated in Figure 3.28. Figure 3.28 (a) exhibits a typical TEM image of pure ZnO sample. Clearly, the product was composed of rod-shaped particles, in accordance with the results obtained by FE-SEM investigation. In order to further investigate the product structure, selected area electron diffraction (SAED) was performed on a single nanorod. The SAED pattern shows a spot pattern, in accordance with the single crystalline wurtzite ZnO structure, indexed to the (100), (102) and (002) planes with electron beam in the [0−10] direction. On the basis of the above results, a possible formation mechanism of ZnO nanorod had been discussed as follows. It has been well known that wurtzite ZnO is described as hexagonal close packing of zinc and oxygen atoms. ZnO crystal structure consists of eight crystallographic planes with different polarity − a positive polar zinc (0 0 1) plane with six symmetric nonpolar (100), (010), (−110), (−100), (0−10) and (1−10) planes parallel to the [0 0 1] direction, and a negative polar oxygen (00−1) plane. Comparing to the

polar zinc (0 0 1) surface, the six nonpolar planes possess lower surface energy and higher stability. Since the system has a tendency to minimize the overall surface energy, thus ZnO crystals preferentially grow along the [0 0 1] direction [77, 78]. TEM image of 3 mol% Gd-doped ZnO presented the nanorod shape product, having similar morphology with pure ZnO. The nanorods have wide size distribution with diameters of 50–80 nm and lengths of 600–1000 nm. The selected area electron diffraction (SAED) was performed on a single nanorod with zone axis of [0−10]. The pattern is in accordance with the single crystalline wurtzite ZnO structure.

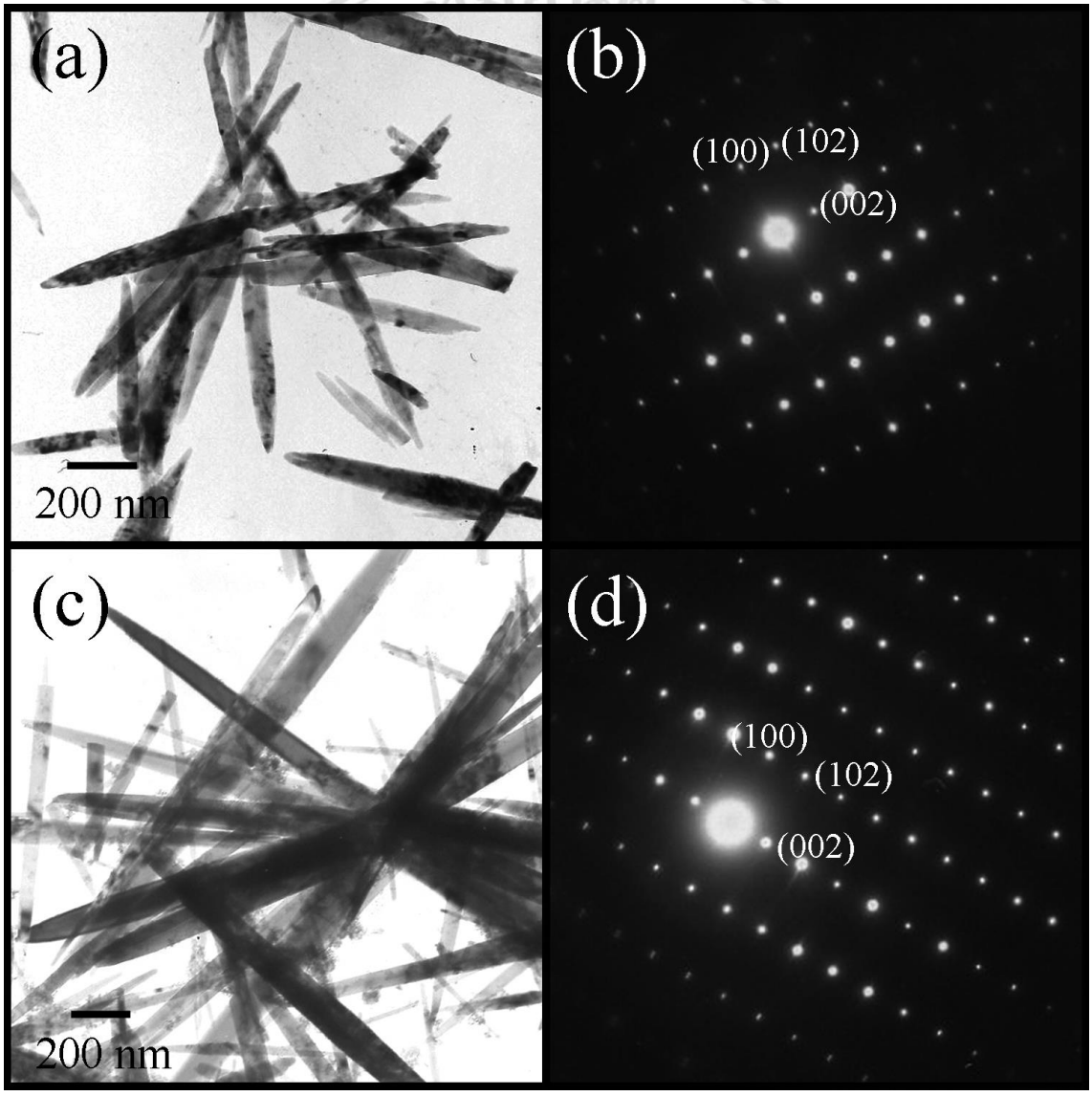

Figure 3.28 TEM images and SAED patterns of (a, b) undoped ZnO, and (c, d) 3 mol% Gd-doped ZnO.

The photocatalytic performance of newly synthesized undoped and Gd-doped ZnO nanorods was evaluated through the degradation of methylene blue (MB). Figure 3.29 shows effects of ZnO and Gd-doped ZnO on the absorbance of MB solution in the presence of UV light. In this research, the MB solutions showed the major absorption peak at 664 nm. First experiment in these series has been carried out under UV light without addition of a photocatalyst in order to evaluate the decomposition of dye due to the direct photolysis. The process was carried out without the photocatalyst and the photolysis test showed no significant change in MB concentration within 300 min. Moreover, MB can be effectively degraded under UV irradiation in the presence of undoped ZnO and Gd-doped ZnO nanorods. The photodegradation of the MB was measured the absorbance at regular interval by a UV-visible spectrophotometer. The intensity of the absorption peak at 664 nm was decreased with the exposure time increase from 0 to 300 min, demonstrating the degradation of organic MB dye by undoped ZnO and Gd-doped ZnO under UV light. They should be noted that the absorption peak of MB performed blue shift from 664 nm to 658 nm during the UV illumination due to the N-demethylation of MB by the photocatalyst in a stepwise manner [79, 80].

The degradation of methylene blue (MB) in the presence of Gd-doped ZnO with different Gd doping contents was measured as the results shown in Figure 3.30 (a). Clearly, Gd-doped ZnO demonstrates higher photocatalytic activities than that of pure ZnO. The photocatalytic activities of the Gd-doped ZnO gradually increased with the increasing in the Gd content, especially, the 3 mol% Gd-doped ZnO exhibited the best performance on the photodegradation of MB.

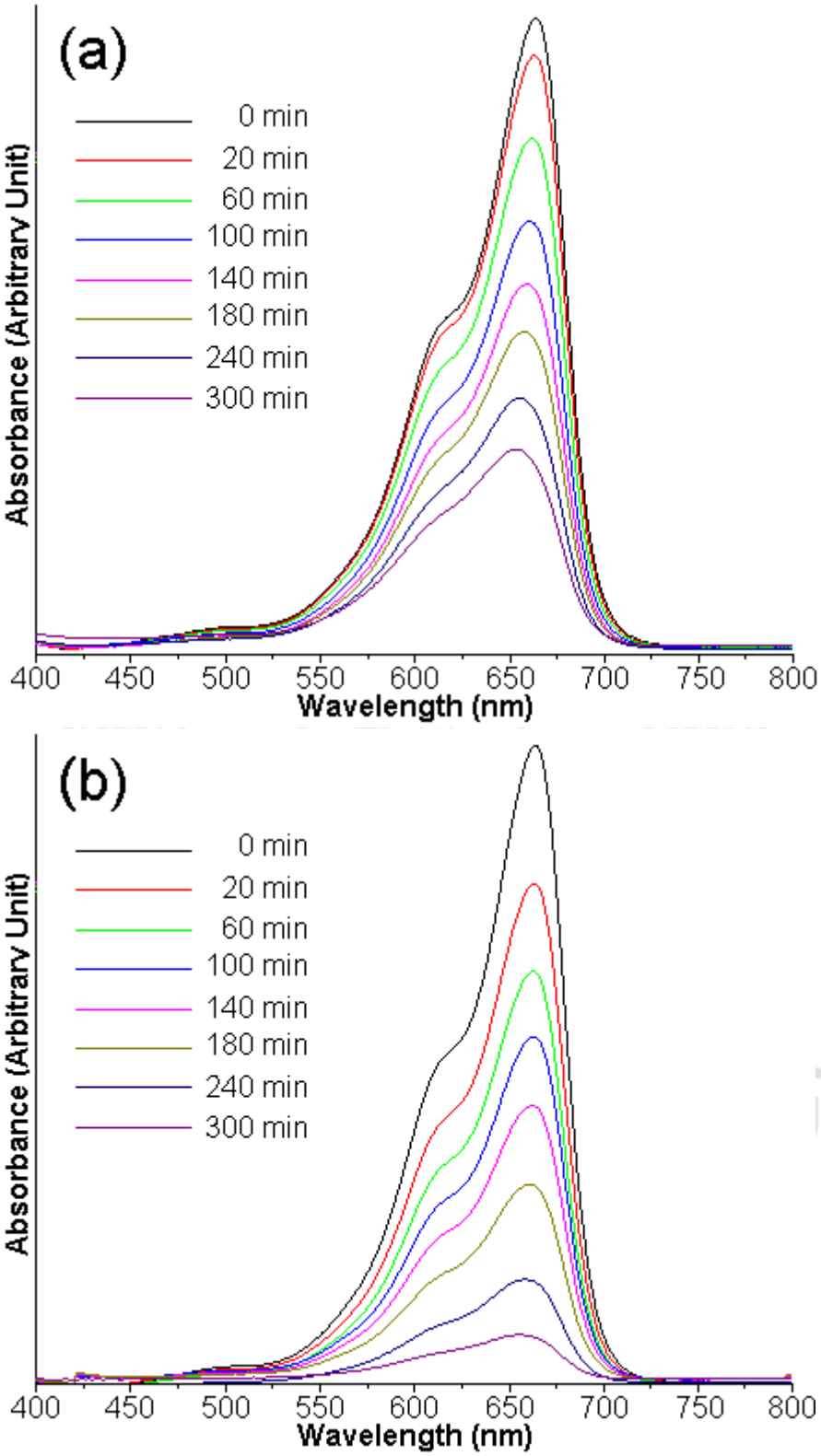

Figure 3.29 UV-visible absorption of MB by UV light irradiation of the solutions containing (a) undoped ZnO and (b) 3 mol% Gd-doped ZnO as the photocatalysts.

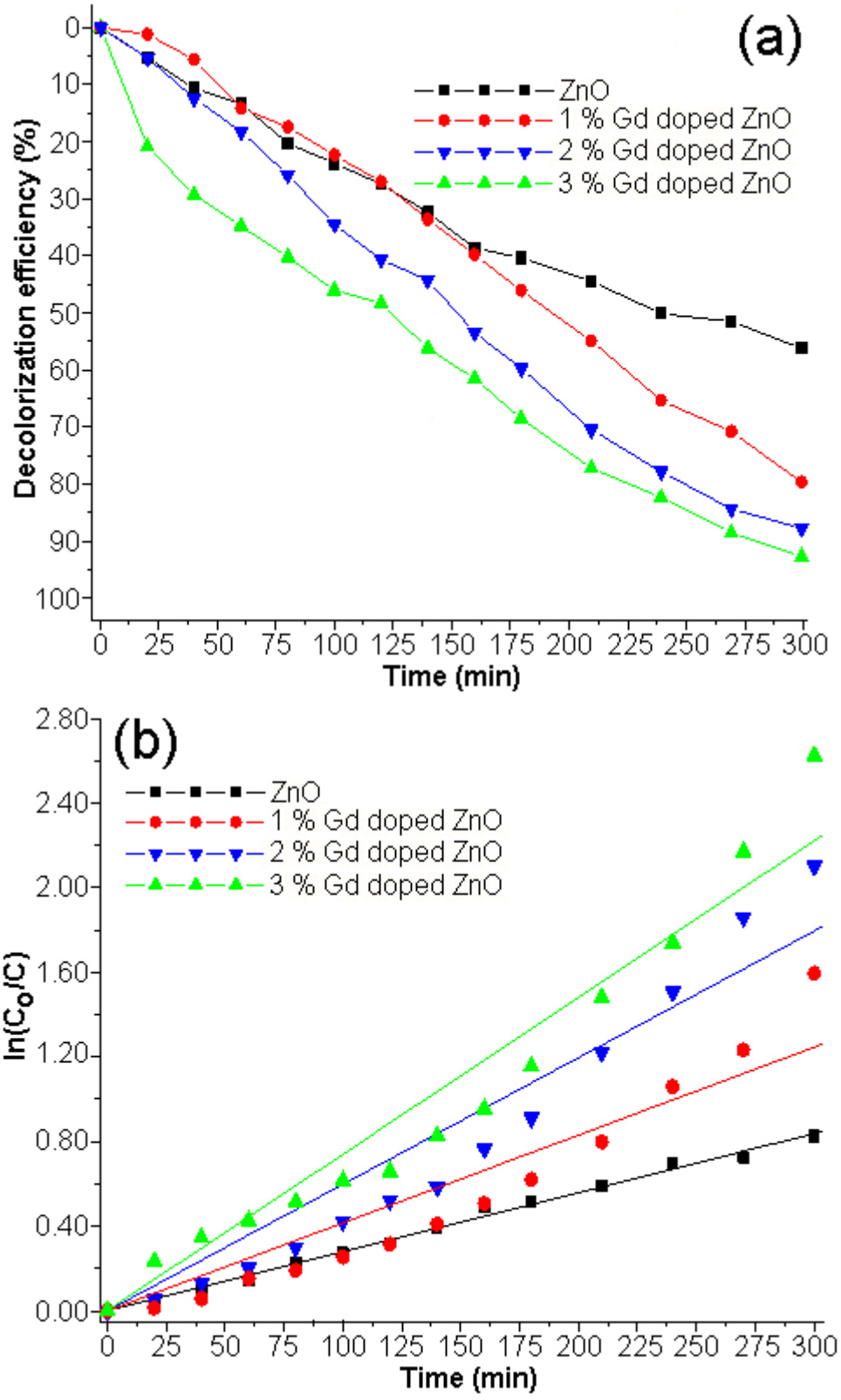

Figure 3.30 (a) Decolorization efficiencies of MB and (b) pseudo-first-order kinetics of the undoped ZnO, and of 1 mol% Gd, 2 mol% Gd and 3 mol% Gd-doped ZnO irradiated with UV light.

Figure 3.30 (b) shows the kinetic degradation of MB over the undoped ZnO and Gd-doped ZnO with different Gd doping contents. In this research, the photocatalytic degradation of MB obeyed the pseudo-first-order kinetics according to the Langmuir-Hinshelwood model [73, 79, 81] related to the adsorption of reactants for the heterogeneous photocatalyst, expressed as

$$\ln(C_o/C) = kt \quad (3.24)$$

, where k is the observed rate constant, C_o is the equilibrium MB concentration and C is the MB concentration within a period of time (t). The relationship between $\ln(C_o/C)$ and irradiation time t corresponded with a linear regression line with $R > 0.99$. Clearly, the k value for the 3 mol% Gd-doped ZnO was 7.53×10^{-3} min^{-1} or 2.72 times larger than the k (2.77×10^{-3} min^{-1}) value for undoped ZnO. For Gd-doped ZnO, the nonlinearity was caused by the increase in surface to volume ratio of Gd-doped ZnO, leading to the increase in exciton formation. This formation could also be increased by longer irradiation time.

Shi et al [82] reported that the photocatalytic performance was controlled by the pH of the dye solution. In acidic solution, the photocatalytic efficiency was lowered because ZnO reacted with acid. In basic solution, the degradation efficiency became higher. Thus, effect of the basicity of dye solution on the photodegradation rate was investigated in this research Figure 3.31 (a). The pH of the MB dye solution containing 3 mol% Gd-doped ZnO before UV radiation was 5.54. At the present stage, the degradation efficiency was 92.76% within 300 min. In the dye solution of more alkaline to reach at the pH of 10, the degradation efficiency was risen to almost 100% within 270 min due to the more negative charged OH^- ions at high basicity solution adsorbed on the surface of 3 mol% Gd-doped ZnO. The OH^- ions containing in the reaction medium favored the formation of hydroxyl $OH^\bullet$ radicals [82–84], which were the advantage for improving the photocatalytic activity of 3 mol% Gd-doped ZnO. In order to know the reusability of the photocatalyst, the degradation experiment was carried out through the optimized condition. The photocatalyst containing in the solution resulting from the photocatalytic degradation of MB was filtered, washed and dried. The dried photocatalyst was reused for the degradation under the same condition. The stability and reusability of 3 mol% Gd-doped ZnO were tested for the degradation of MB in the dye solution with the pH of 10 for four cycles (Figure 3.31 (b)). It can be seen that the

degradation efficiency of 3 mol% Gd-doped ZnO was slightly decreased to 98.70% after four cycles' past. These results indicated that 3 mol% Gd-doped ZnO was stable and reusable under UV light.

For comparison, the photocatalytic degradation of MB solutions with the pH of 5.54 and 10 by the 3 mol% Gd-doped ZnO under visible irradiation was tested and evaluated (Figure 3.32 (a)). The MB solution with the pH of 10 was degraded to almost 100% within 160 min by 3 mol% Gd-doped ZnO under visible irradiation. For the MB solution without pH adjusting, the degradation was only about 90% due to the less amount of OH^- adsorbed on the surface of 3 mol% Gd-doped ZnO. The presence of large amount of OH^- ions on the photocatalytic surface as well as in the reaction medium favors the formation of reactive $OH^\bullet$ radicals as oxidizing agent [82-84]. The recycling photocatalytic experiment was tested by reusing the 3 mol% Gd-doped ZnO in the solution with the pH of 10 for four cycles as shown in Figure 3.31 (b). The MB degradation efficiency was decreased from 99.47% of first cycle to 98.53% of the fourth one. A slight decrease of the degradation efficiency confirmed that the photocatalyst was very stable.

When the photocatalyst is irradiated with radiation (UV or visible), electrons in the valence band (VB) diffuse to the conduction band (CB), leading to the formation of the same number of holes in the VB and initiating a series of reaction to produce hydroperoxyl radicals ($^\bullet HO_2$) and hydroxyl radicals ($^\bullet OH$). These radicals are strong oxidants and can decompose organic pollutants. During the process, an undesirable recombination of electrons and holes in the pure ZnO photocatalyst may rapidly proceed, reducing the photocatalytic activity. The Gd^{3+} dopant is ready to trap the electrons in the conduction band by transforming Gd^{3+} into Gd^{2+}. Electrons of the nascent Gd^{2+} may diffuse to the nearby dissolved O_2 to form superoxide radical anions ($^\bullet O_2^-$). Thus the recombination of photoinduced electrons and holes is inhibited. In the present research, the Gd^{3+} on the surface of ZnO acts as an electron scavenger. Energy gap of Gd^{3+} doped ZnO is wider than the energy gap of pure ZnO, leading to the more electron–hole stability and favor photocatalytic degradation efficiency [85–87].

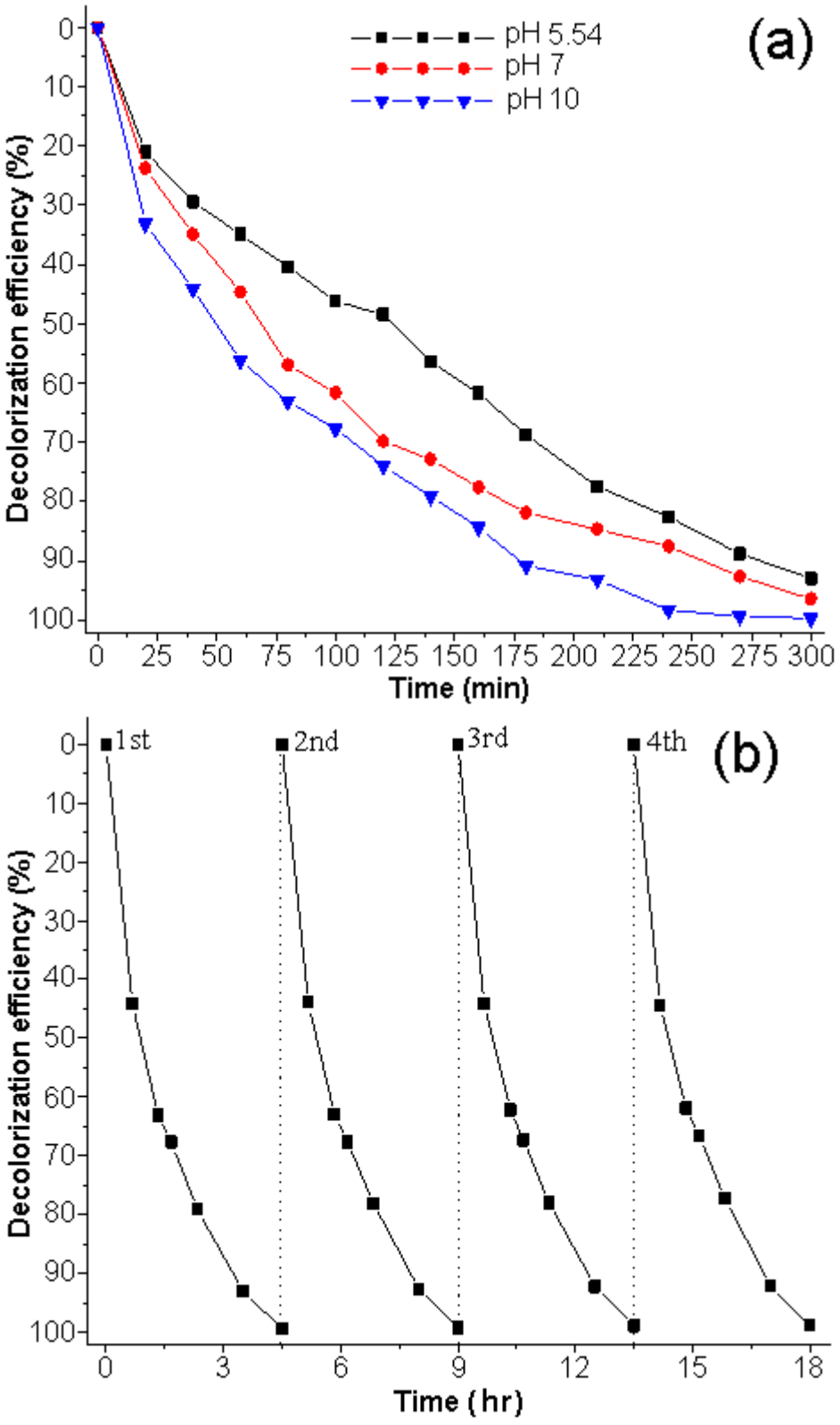

Figure 3.31 Decolorization efficiencies of MB in the different solutions: (a) pH = 5.54, 7 and 10 by 3 mol% Gd-doped ZnO and (b) pH = 10 by the recycled 3 mol% Gd-doped ZnO irradiated with UV light.

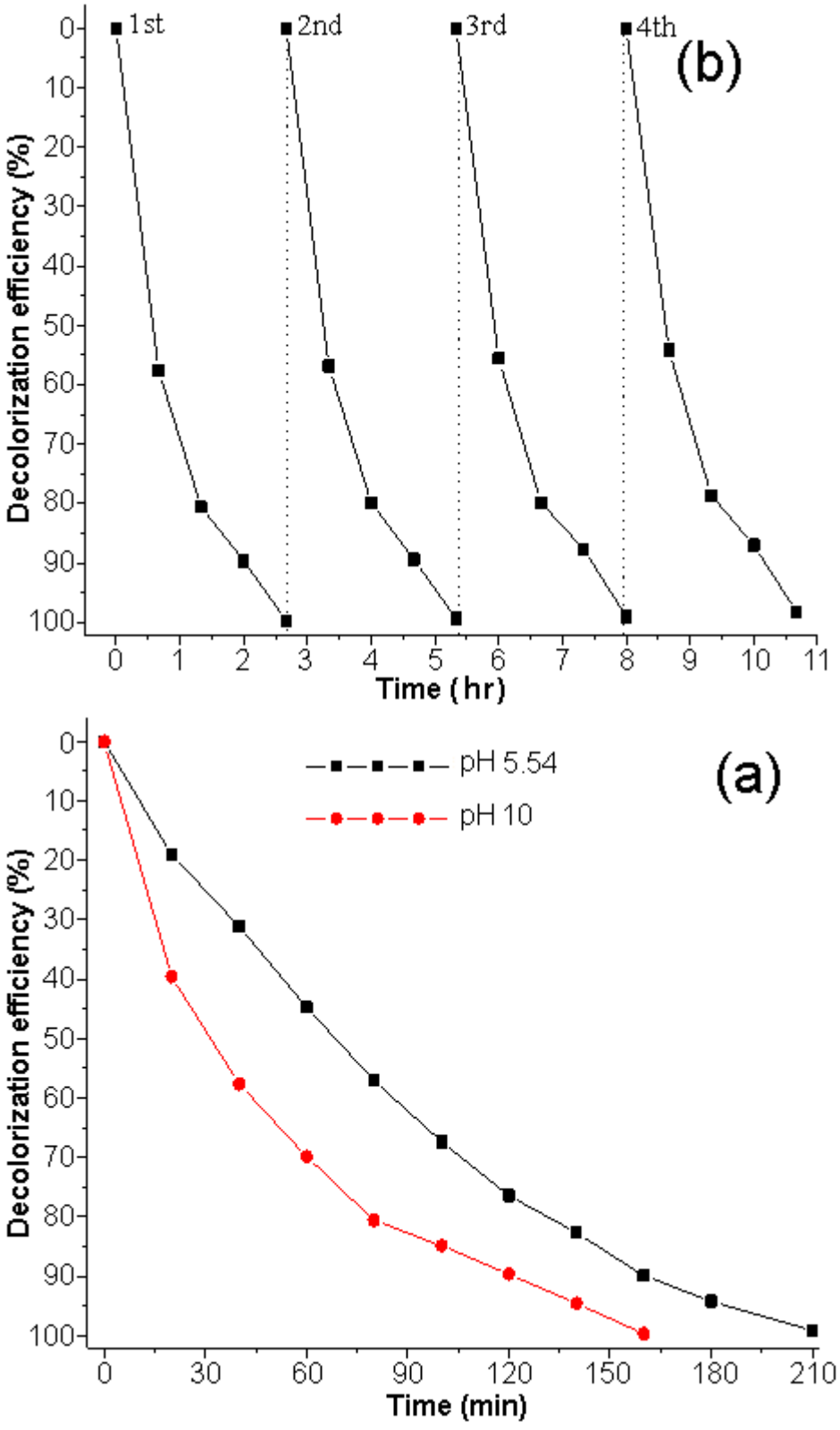

Figure 3.32 Decolorization efficiencies of MB in the different solutions: (a) pH = 5.54 and 10 by 3 mol% Gd-doped ZnO and (b) pH = 10 by the recycled 3 mol% Gd-doped ZnO irradiated with visible light.